THE ASTROPHYSICAL JOURNAL, 440:28–47, 1995 February 10

BRIGHTEST CLUSTER GALAXIES AS STANDARD CANDLES

MARC POSTMAN[1]
Space Telescope Science Institute,[2] 3700 San Martin Drive, Baltimore, MD 21218
AND
TOD R. LAUER[3]
Kitt Peak National Observatory, National Optical Astronomy Observatories, P.O. Box 26732, Tucson, AZ 85726
Received 1994 June 7; accepted 1994 August 15

ABSTRACT

We investigate the use of brightest cluster galaxies (BCGs) as standard candles for measuring galaxy peculiar velocities on large scales. We have obtained precise large-format CCD surface photometry and redshifts for an all-sky, volume-limited ($z \leq 0.05$) sample of 119 BCG. We reinvestigate the Hoessel (1980) relationship between the metric luminosity, L_m, within the central 10 h^{-1} kpc of the BCGs and the logarithmic slope of the surface brightness profile, α. The L_m-α relationship reduces the cosmic scatter in L_m from 0.327 mag to 0.244 mag, yielding a typical distance accuracy of 17% per BCG. Residuals about the L_m-α relationship are independent of BCG luminosity, BCG $B-R_c$ color, BCG location within the host cluster, and richness of the host cluster. The metric luminosity is independent of cluster richness even before correcting for its dependence on α, which provides further evidence for the unique nature of the BCG luminosity function. Indeed, the BCG luminosity function, both before and after application of the α-correction, is consistent with a single Gaussian distribution. Half the BCGs in the sample show some evidence of small color gradients as a function of radius within their central 50 h^{-1} kpc regions but with almost equal numbers becoming redder as becoming bluer. However, with the central 10 h^{-1} kpc the colors are remarkably constant—the mean $B-R_c$ color is 1.51 with a dispersion of only 0.06 mag. The narrow photometric and color distributions of the BCGs, the lack of "second-parameter" effects, as well as the unique rich cluster environment of BCGs, argue that BCGs are the most homogeneous distance indicators presently available for large-scale structure research.

Subject headings: galaxies: clusters: general — galaxies: photometry

1. INTRODUCTION

We have recently completed a program to measure the motion of the Local Group with respect to a full-sky sample of Abell clusters (Lauer & Postman 1994, hereafter Paper I). Our goal was to explore galaxy bulk flows on much larger scales than had been done previously. Central to our investigation was the use of the luminosities of brightest cluster galaxies (BCGs) as distance indicators. BCGs had heretofore yielded conflicting results on large-scale peculiar motions (Sandage 1975; James, Joseph, & Collins 1987; Lucey & Carter 1988) because of heterogeneous data quality, small sample sizes, and the lack of full-sky coverage. However, we were impressed enough by the properties of BCGs to choose their use over the more conventional Tully-Fisher and D_n-σ methods. First, the BCGs as a class are probably more homogeneous than all other types of galaxies used as distance indicators. Second, the BCGs could be readily identified over the full sky from digitized sky surveys by looking in the vicinities of clusters in the Abell (1958) and Abell, Corwin, & Olowin (1989; hereafter ACO) catalogs out to distances well in excess of our 15,000 km s^{-1} survey limit. Further, since the BCGs reside at the center of rich clusters, their individual peculiar velocities are minimized and their selection is largely invulnerable to inhomogeneous Malmquist bias. Their photometric homogeneity also minimizes homogeneous Malmquist bias, as well as concerns over undiscovered biases due to possible "second parameters." Last, use of BCGs is relatively easy; only photometric images and "redshift" quality spectra are required, in contrast to the Tully-Fisher and D_n-σ methods, which require higher signal-to-noise "dispersion" quality spectroscopic observations.

Humasom, Mayall, & Sandage (1956) first identified the photometric homogeneity of BCGs, leading to the work of Sandage (1972a, b), who explored in detail the use of BCGs as cosmological probes. A key aspect of this work was a demonstration that the luminosities of the BCGs had an impressively small dispersion of 0.25 mag, after correction for a relationship between BCG luminosity and cluster morphology, and careful culling of the data. Gunn & Oke (1975) presented a somewhat different formulation of the BCG distance scale, focusing on the metric luminosity, L_m of the BCGs within a physical aperture, r_m, of relatively small size compared to the extent of the BCGs. In this case, BCGs cannot be treated as point sources; errors in luminosity are related to errors in distance by α, the logarithmic slope of L_m as a function of r_m. Hoessel (1980) further showed the existence of a relationship between L_m and α that could be used to both reduce the luminosity scatter of BCGs as well as to counter some selection effects. Unfortunately, the L_m-α relationship measured from the more modern photometry of Hoessel & Schneider (1985) was poorly defined, showing little improvement over the scatter in L_m alone.

We have selected the 119 BCGs in the present sample to define an inertial frame suitable for measuring the motion of the Local Group (see Paper I for results). The sample covers all

[1] Visiting Astronomer, Kitt Peak National Observatory (KPNO) and Cerro Tololo Inter-American Observatory (CTIO), National Optical Astronomy Observatories. NOAO is operated by the Association of Universities for Research in Astronomy (AURA), Inc., under cooperative agreement with the National Science Foundation.

[2] Space Telescope Science Institute is operated by AURA, Inc., under contract to the National Aeronautics and Space Administration.

[3] Visiting Astronomer, CTIO.

the sky with $|b| \geq 15°$ and is volume limited, in contrast to the previous BCG studies listed above, which were incomplete and largely based on galaxies observable from the north. Our program imposed stringent requirements on the photometric accuracy of our imaging data. Specifically, a 3 σ detection of a 600 km s^{-1} bulk velocity on a scale of 15,000 km s^{-1} demands that any total systematic error in galaxy magnitudes be limited to $\lesssim$0.02 mag. A key component of the measurement of the Local Group motion presented in Paper I is, thus, the primary topic of this paper—a precise recalibration of the $z \approx 0$ photometric properties of the central regions of BCGs and a full assessment of their status as standard candles.

We find the metric luminosity, L_m, of the central 10 h^{-1} kpc regions of BCGs within $z \leq 0.05$ to be independent of their $B-R_c$ color, their location within the host cluster, and the richness of the host cluster. We confirm the Hoessel (1980) L_m-α relationship, finding that the cosmic scatter in L_m is significantly reduced when its dependence on the logarithmic slope of the surface brightness profile, α, is accounted for. The residuals between the observed L_m and the metric luminosity predicted from the L_m-α relationship contain distance information and are shown to be independent of BGC luminosity, BCG color, and cluster parameters. These observations support the hypothesis that the central regions of BCGs are composed from quite similar stellar populations and, thus, validate their use as standard candles and as probes of the large-scale kinematics of the local universe.

The sample selection process is summarized in § 2. The data acquisition and reduction are described in § 3. Section 4 contains the full description of our BCG distance indicator and the various correlations between the photometric properties of the BCGs as well as between these properties and the properties of the host clusters. Our conclusions are in § 5.

2. SAMPLE SELECTION

2.1. *The Abell Cluster Sample*

We began by selecting for possible observation all Abell or ACO clusters (i.e., no richness class limits) with measured or photometrically estimated heliocentric redshifts $\lesssim$15,000 km s^{-1} and galactic latitude $|b| \geq 15°$. These criteria yielded a sample of 153 clusters. Of these 153 clusters, 22 ultimately turned out to have $z > 0.05$—incorrect previously measured redshifts were always cases where the cluster redshift was based on only one galaxy that we discovered to be in the foreground. Because the L_m-α distance indicator is strictly applicable to old stellar systems, we further restrict our observations to elliptical BCGs. Consequently, we exclude from the present analysis four of the clusters which have spiral BCGs (A2995, A3354, A3578, and A3816). In addition, A426 is excluded given the well-known A-type spectrum of its BCG, NGC 1275. There are six Abell and ACO "clusters" (A34, A256, A480, A762, A3388, and A3990) which were not observed. This is because there is no apparent overdensity we can identify on the POSS or SERC plates at the reported coordinates that is consistent with the indicated richness and estimated or previously measured redshift. A400 and A3555, while within the redshift cutoff, are not used in this analysis because they have anomalously faint ($\sim$4 σ deviation) BCGs. A2295 and A3577 are also within the redshift cutoff, but the spectroscopic observations were unfortunately obtained after the conclusion of our imaging runs and hence no CCD image data are available.

We included three clusters (A3528, A3530, and A3532) from the "apparent" background of the very rich Shapley concentration that are nominally outside the 15,000 km s^{-1} redshift cutoff because they may indeed be within the volume, given plausible infall velocities around this supercluster. The Shapley supercluster is the only large enhancement in the cluster distribution which straddles our survey redshift limit (mean heliocentric redshift = 14,567 km s^{-1}). The next nearest large supercluster is a five-member system (mean heliocentric redshift = 16,670 km s^{-1}) located in the Leo supercluster complex (Tully 1987). This sytem is substantially less rich than the Shapley supercluster (which has 11 members at the same percolation length), and, consequently, the probable infall velocities are smaller and it is unlikely that any of the member clusters are really within the survey volume.

The final sample consists of 119 clusters and is given in Table 1. We emphasize that the exclusion of 32 of the 35 clusters discussed above is based solely on redshift, the lack of a significant overdensity, or nonelliptical BCG morphology. All cluster and BCG velocities given in Table 1 are heliocentric. The cluster space density is nearly constant out to 15,000 km s^{-1}, indicating that the sample is effectively volume limited (see Fig. 3 in Paper I). A Kolmogorov-Smirnov (K-S) test comparing the observed redshift distribution with that expected for a volume-limited survey yields a probability of 0.74 that the cluster sample is indeed volume limited. This is an especially attractive feature of the sample as distance-dependent biases are minimized or eliminated. The overdensity at $\sim$4500 km s^{-1} is a $\lesssim$2 σ fluctuation due to the Hydra-Centaurus supercluster. The prominence of this fluctuation is amplified because there are only 13 Abell and ACO clusters with $z \leq 0.02$.

2.2. *The Brightest Cluster Galaxy Selection*

We performed our own BCG selection for each cluster. This was necessary because accurate positions of BCGs in most of the southern ACO clusters were not available in the literature and because we wanted to eliminate scatter in the distance indicator due to galaxies incorrectly identified as BCGs by previous investigators. This latter consideration does in fact appear to be important, as in a number of cases we have selected different galaxies from those that Hoessel, Gunn, & Thuan (1980) did for the same clusters (see the notes to Table 1).

Our first pass at BCG selection was done from 14.5 × 14.5 images extracted from the STScI digitized Schmidt plate database, centered on the cluster positions given in the Abell and ACO catalogs. For clusters north of the celestial equator, the plate material came from the Palomar Quick V Survey (QV; epoch 1983). For clusters south of the celestial equator, the plate material came from the UK Schmidt SERC J Survey (SERC-J epoch 1975). Both surveys were digitized using the PDS microdensitometers at STScI during construction of the *Hubble Space Telescope* (*HST*) Guide Star Catalog (Lasker et al. 1990). The image pixel size in all cases is 1.7 (25 μm). The plate limits are $V \approx 19$ and $J \approx 21$ for the QV and SERC-J surveys, respectively, more than sufficient to assure complete BCG identification out to $z = 0.05$.

We selected BCG candidates by eye, but we also computed instrumental magnitudes of the galaxies from the plates to aid our decisions. We relied on redshift data (where available) as well to eliminate foreground galaxies. In cases where two BCG candidates in the same cluster could not be ranked unambiguously (primarily due to saturation effects), we obtained CCD data for both. There were no clusters in our sample with more than two BCG candidates.

TABLE 1

THE BCG SAMPLE

Abell	R.A. (J2000)	Dec	BCG cz	Cluster cz	Runs	Notes
76	00 39 26.32	+06 44 02.5	11162	11162	2	I1565
119	00 56 16.13	−01 15 22.1	13320	13354	2, 3	
147	01 08 37.90	+02 16 06.1	13138	13022	2	Note 1
160	01 12 59.76	+15 29 29.3	13095	13095	2	
168	01 14 57.70	+00 25 52.1	13439	13446	2, 3	Note 1
189	01 23 26.33	+01 42 17.8	10236	9925	2	
193	01 25 07.54	+08 41 57.0	14825	14553	2	I1695
194	01 25 58.84	−01 20 21.8	5321	5357	2	N 545
195	01 26 54.75	+19 12 50.1	12796	12796	2, 3	I 115
260	01 50 42.96	+33 04 54.8	10699	10998	2	
261	01 51 26.48	−02 15 11.5	13965	13965	3	
262	01 52 46.28	+36 09 05.3	4831	4913	2	N 705
295	02 02 17.24	−01 07 40.6	12818	12890	2, 3	
347	02 25 26.47	+41 49 27.1	5257	5604	2	N 910
376	02 46 04.04	+36 54 16.7	14700	14700	2	
397	02 56 28.91	+15 54 58.9	10286	9975	2	
407	03 01 51.60	+35 50 27.4	14059	14130	2	
419	03 08 28.73	−23 36 53.2	12240	12240	2	Note 2
496	04 33 37.68	−13 15 39.7	9893	9893	1, 2, 3, 4	
533	05 01 08.25	−22 34 58.1	14365	14149	2, 3, 5	
539	05 16 55.12	+06 33 09.5	9682	8754	2, 3, 4	
548	05 49 21.74	−25 20 47.0	11848	11949	1, 2, 5	
569	07 09 07.76	+48 36 55.3	5724	5749	2, 4	N2329
576	07 22 06.83	+55 52 29.3	12072	11542	4	
634	08 15 44.90	+58 19 15.8	8135	8135	4	
671	08 28 31.92	+30 25 48.0	14970	15219	4	I2378
779	09 19 46.80	+33 44 58.7	6867	6796	4	N2832
912	10 01 09.41	−00 04 46.5	13572	13572	3, 4, 5	
957	10 13 38.27	−00 55 31.3	13438	13433	3, 4, 5	
999	10 23 23.85	+12 50 05.8	9749	9603	4	
1016	10 27 07.91	+11 00 36.9	9705	9669	4	I 613
1060	10 36 42.56	−27 31 42.9	3704	3719	5	N3311
1100	10 48 45.73	+22 13 03.4	13990	13990	4	
1139	10 58 11.02	+01 36 15.4	11460	11788	4	U6057, Note 3
1142	11 00 45.39	+10 33 11.6	10118	10501	4	I 664
1177	11 09 44.52	+21 45 31.5	9561	9561	4	
1185	11 10 38.32	+28 46 03.0	10521	9917	4	N3550
1213	11 16 22.87	+29 15 08.1	13535	14045	4	Note 1
1228	11 21 23.19	+34 21 24.4	10674	10973	4	
1257	11 25 31.10	+35 30 15.3	10220	10297	4	Note 1
1267	11 28 36.40	+26 54 19.4	9798	9830	4	
1308	11 33 05.09	−04 00 49.8	15508	15508	4	
1314	11 34 49.42	+49 04 38.3	9977	9838	4	I 712
1367	11 44 02.17	+19 56 58.7	6237	6469	4	N3842
1631	12 53 18.20	−15 31 58.0	14275	14030	4	Note 4
1644	12 57 11.76	−17 24 35.0	14237	14220	4, 5	
1656	13 00 08.04	+27 58 36.3	6497	6961	4	N4889
1736	13 27 28.04	−27 19 27.6	13605	13583	4	I4252
1836	14 01 41.84	−11 36 22.7	10999	11036	4, 5	
1983	14 52 43.25	+16 54 12.9	13756	13617	4	Note 1
2040	15 12 47.74	+07 26 02.0	13680	13698	4	
2052	15 16 44.55	+07 01 16.8	10331	10575	4	
2063	15 23 05.46	+08 36 33.2	10626	10633	4, 5	
2107	15 39 39.05	+21 46 55.7	12613	12496	4	U9958
2147	16 02 17.04	+15 58 27.6	10384	10511	4, 5	
2151	16 04 35.76	+17 43 18.0	11248	11115	5	N6041
2152	16 05 29.28	+16 26 11.0	13598	13598	4, 5	
2162	16 12 35.73	+29 29 03.5	9547	9629	5	N6086
2197	16 29 45.04	+40 48 42.5	8800	9042	4	N6173, Note 1
2199	16 28 38.45	+39 33 03.0	9348	9034	4	N6166
2247	16 52 48.08	+81 37 57.9	12016	11641	4	
2572	23 17 13.54	+18 42 28.2	13009	12420	2	
2589	23 23 57.55	+16 46 35.8	12144	12397	2	
2593	23 24 20.15	+14 38 50.4	12514	12489	2	N7649
2634	23 38 29.44	+27 01 49.7	9141	9153	2	N7720
2657	23 44 30.49	+09 15 51.6	12454	12100	4	Note 1
2666	23 50 58.66	+27 08 47.6	8123	8057	2	
2717	00 03 12.77	−35 56 16.7	14936	14753	1	
2731	00 09 59.04	−57 01 17.7	9457	9457	1	N 25
2806	00 40 48.47	−56 12 53.4	8229	8252	1	N 215
2870	01 07 41.84	−46 54 31.2	6714	7233	1, 3	I1625
2877	01 09 54.82	−45 55 57.3	7261	7309	3	I1633
2881	01 11 14.14	−17 04 14.5	13363	13324	2	
2896	01 18 18.60	−37 06 17.0	9555	9555	3	
2911	01 25 12.19	−38 05 38.0	5992	6056	3	N 544
3144	03 37 04.88	−55 01 20.8	13120	13546	3	
3193	03 58 13.54	−52 19 44.4	10009	10350	1, 3	
3367	05 49 41.71	−24 32 43.7	13461	13461	2, 3	
3374	05 56 42.97	−21 15 12.4	14201	14307	2, 3	

TABLE 1—*Continued*

Abell	R.A. (J2000)	Dec	BCG cz	Cluster cz	Runs	Notes
3376	06 00 41.01	−40 02 46.6	13814	13907	1, 3	
3381	06 09 53.76	−33 35 34.1	11488	11467	1, 3	
3389	06 22 21.30	−64 56 04.6	8294	8114	1, 3	
3395	06 27 36.42	−54 27 01.7	14520	14712	3	
3526	12 48 48.94	−41 18 42.0	3045	3454	5	N4696
3528	12 54 22.31	−29 00 45.9	16425	16317	5	Note 5
3530	12 55 36.10	−30 20 49.3	16162	16206	5	Note 5
3532	12 57 22.15	−30 21 47.5	16633	16646	5	Note 5
3537	13 01 00.71	−32 26 28.9	5104	5053	5	
3542	13 08 41.52	−34 34 31.3	10389	10387	5	
3553	13 19 15.08	−37 10 46.5	14446	14446	5	
3554	13 19 31.53	−33 29 19.7	14333	14333	5	
3556	13 24 06.76	−31 40 15.0	14459	14500	5	
3558	13 27 56.53	−31 29 46.8	14110	14312	5	
3559	13 29 51.02	−29 30 53.1	14105	14213	5	
3560	13 31 53.33	−33 14 04.4	3644	3734	5	N5193
3562	13 33 34.74	−31 40 20.3	14708	14708	5	
3564	13 34 55.37	−35 05 57.8	14496	14721	5	
3565	13 36 39.06	−33 57 56.7	3762	3834	5	I4296
3566	13 39 38.22	−35 36 32.6	14529	14529	5	
3570	13 46 24.00	−37 58 15.5	11377	11156	5	
3571	13 47 28.42	−32 51 51.8	11679	11913	5	
3572	13 48 14.26	−33 22 57.8	12134	12141	5	
3574	13 49 05.29	−30 17 44.9	4523	4657	5	I4329
3575	13 52 38.36	−32 53 17.3	11188	11188	5	
3581	14 07 29.51	−27 01 07.0	6618	6682	5	I4374
3656	20 00 49.97	−38 34 35.9	5965	5768	3, 5	I4931
3676	20 24 24.50	−40 21 59.5	12108	12108	3	
3677	20 26 23.56	−33 21 03.5	13787	13789	3	
3698	20 35 56.21	−25 16 45.3	5799	6040	3	N6936
3716	20 51 56.82	−52 37 47.9	13900	13426	3, 5	
3733	21 01 59.07	−28 03 34.5	10943	11039	1, 3	
3736	21 05 04.49	−43 25 09.2	14604	14604	3	
3742	21 07 52.28	−47 10 43.4	4764	4842	3	N7014
3744	21 07 16.19	−25 28 08.4	11041	11153	3	
3747	21 08 38.93	−43 29 11.1	9174	9170	1, 3	
3869	22 20 31.05	−55 07 29.9	12005	12005	3	N7249
4038	23 47 28.30	−28 06 34.6	8218	8501	3	I5353
4049	23 51 36.65	−28 21 55.7	8137	8512	1	I5362
4059	23 57 00.37	−34 45 32.4	14696	14730	3	

NOTE.—All velocities are heliocentric and are given in km s^{-1}. (1) The present BCG choice differs from the galaxy selected by Hoessel et al. 1980. (2) A0419 appears to consist of two overlapping clusters at $z = 0.041$ and $z = 0.068$. We have selected the lower redshift component. (3) The redshift for the BCG in A1139 (obtained from the CfA Redshift Survey) had a relatively large measurement error of 170 km s^{-1} (see Table 6). However, a remeasurement of its redshift by us in 1992 gives a heliocentric velocity of 11,495 (±29) km s^{-1}, within 35 km s^{-1} of the less precise value. (4) A1631 appears to consist of two overlapping clusters at $z = 0.014$ and $z = 0.046$. We have selected the higher redshift component. (5) This cluster was included to test for inhomogeneous velocity bias at the sample edge (see Paper I).

To back up our first pass at BCG selection, we inspected the QV and SERC-J Schmidt plate prints directly by eye out to a projected radius of 5 h^{-1} Mpc ($\sim 2°$ at $z = 0.05$) to identify candidate BCGs lying just beyond the initial 14.′5 field boundaries. To facilitate this step, we created transparent overlays of the positions of all CfA Catalog redshifts within the projected area (Huchra 1991; Huchra et al. 1992). There are 18 clusters (14.5% of the sample) with BCGs that lie beyond our initial 14.′5 field. In these cases, a second digitized image was extracted and the instrumental magnitude was computed to verify the selection.

Our final BCG identifications are strictly based on the CCD photometry discussed in the next section and consistency between the BCG redshift and the mean cluster redshift. We emphasize that the designation of "brightest galaxy" is thus based only on the metric magnitudes presented below, rather than on estimated total magnitudes. Indeed, in a few cases, the identity of the BCGs would change if a much larger aperture size were used. Our strict definition of the BCGs also means that we considered all galaxies regardless of their location within a 5 h^{-1} Mpc projected radius from the cluster center. In the Virgo Cluster, for example (which is not in our sample), we would have selected NGC 4472 over NGC 4486, despite the latter's more central location and extensive X-ray halo. In our sample, the median projected BCG separation from the published center of its host cluster is 70 h^{-1} kpc, 90% of the BCGs lie within a projected radius of 350 h^{-1} kpc, and the largest projected BCG separation as 1.2 h^{-1} Mpc (A548).

There are no significant differences in the BCG properties between clusters selected from the original Abell catalog and clusters selected from the ACO southern hemisphere extension. The metric luminosities, colors, and profile shapes are consistent with being drawn from the same universal distributions.

The positions of all BCG candidates were computed using the astrometric solutions provided by version 1.0 of the *HST* Guide Star Catalog. A center-of-gravity algorithm was used to compute the centroid in a 15″ × 15″ box centered on the peak pixel. The J2000 BCG positions are given in Table 1. All positions have absolute errors less than 1.″5.

3. OBSERVATIONS AND REDUCTION

3.1. *Photometry*

3.1.1. *Imaging Observations and Basic Reduction*

CCD Images of the BCGs were acquired under photometric conditions using the KPNO 4 m and 2.1 m telescopes, and the CTIO 1.5 m telescope between 1989 November and 1991 April (over a total of five observing runs). Images were obtained in the Kron-Cousins R_c band, which we use as the primary bandpass of the photometric distance indicator. We also imaged all but 13 of the galaxies in the Johnson B band to provide color information. Table 2 summarizes the runs and CCD detectors used.

The exposure times were typically 200–600 s and were set by the desire that the R_c-band CCD images have signal-to-noise ratios (S/Ns) of at least 100 in the central pixels of the BCGs. While this number is somewhat arbitrary, high-S/N images allow the best identification and removal of galaxies or other objects that contaminate the BCG envelopes. The BCGs are quite red, and we accept a lower S/N (typically 40–50) for our B-band images, as these are not directly used to estimate cluster distances.

Dome flats and blank night-sky frames were obtained to flatten the images. Our R_c-band frames typically could be flattened to better than 0.5% of the sky level. Background sky levels were measured from the pixel intensity modes in the image corners. For the most extended BCGs, where we were concerned that galaxy light might contribute to the sky, we obtained images offset from the nominal pointing to sample the sky at larger angular distances from the galaxies. The offset frames overlapped with the BCG images, thus allowing direct measurement of the amount of galaxy-light contamination, independent of any global fluctuations of the sky that might have occurred between the two images.

3.1.2. *Measurement of the Aperture Photometry*

The BCG distance indicator is based on the integrated luminosity of the galaxy through an aperture of constant physical

TABLE 2

BCG IMAGING RUNS

Run	Date	Telescope	CCD	Pixel Scale	FOV
1.....	1989 Oct	CTIO 1.5 m	TI 800 × 800 (TI2)	0.″273	3.′6
2.....	1989 Nov	KPNO 4 m	TI 800 × 800 (TI2)	0.299	4.0
3.....	1990 Nov	CTIO 1.4 m	TI 800 × 800 (TI2)	0.273	3.6
4.....	1991 Mar	KPNO 2.1 m	Tek 1024 × 1024 (TE1K)	0.304	5.2
5.....	1991 Apr	CTIO 1.5 m	Tek 1024 × 1024 (TEK1K-1)	0.434	7.4

size, with a correction based on the logarithmic slope, α, of the curve of growth at the edge of the aperture. Because we wanted to investigate the best aperture size to use and, further, were likely to vary the *angular* size of the aperture as we iteratively derived the Local Group motion, we represented the photometry of each BCG as a set of apparent magnitudes measured through apertures of increasing geometric size, rather than just the flux through any fiducial aperture. We then used a spline both to interpolate between the apertures and to measure the local α at any desired radius.

Measurement of the aperture curve of growth proceeded in two steps. The first step was to extract the surface brightness profile of the BCG. Since other cluster galaxies are often interacting with or projected against the envelope of the BCG, it was necessary to decompose such composite systems into their individual glaxies. We did this using the multi-isophote decomposition algorithm of Lauer (1986), which can solve for the brightness distributions of several overlapping galaxies in a simultaneous least-squares fit. Compact contaminating objects, such as stars, can also be excluded from the fit. The decomposition algorithm recovers the galaxy brightness distributions only under the assumption that the isophotes of each system are concentric and elliptical; no model of the brightness profile is assumed and isophote position angle is allowed to vary.

Implicit in this approach is identification of the BCG as the dominant component in a composite system. Since 75% of multiple systems are only chance superpositions of cluster galaxies, or result from high-speed nonmerging encounters (Lauer 1988), this procedure is likely to be sensible. We thus contrast our method with that of Schneider, Gunn & Hoessel (1983a), who view the whole system as the BCG, adopting the luminosity centroid as the center of the apertures.

The multi-isophote decomposition is especially important for $\sim$30 of the 119 BCGs because the flux contribution from non-BCG galaxies is $\geq$0.02 mag within the metric aperture. The observed L_m-α relationship and the scatter about it do not change significantly if we exclude these 30 galaxies from our analysis. We note in passing that exclusion of these 30 BCGs also does not significantly affect the derived dipole solution given in Paper I. The results of this exclusion test provide further assurance that our photometric measurement procedure is not introducing artificial signals into the data.

The aperture photometry itself is measured from the model BCG light distribution reconstructed from the measured surface photometry. The R_c-band photometry and $B-R_c$ color (prior to correction for extinction and K-dimming) for each BCG is given in Table 3 as a function of geometrically increasing aperture radius in arcseconds. The second aperture given is always the adopted metric aperture, calculated for the cluster redshifts given in Table 1, under the assumption that the Local Group is at rest with respect to the Abell cluster inertial frame. Where multiple observations of the given BCG exist, they have been averaged. Last, since the B-band images are shallower than the R_c images, for a number of galaxies we provide colors for only the inner apertures.

3.1.3. *Photometric Calibration*

The photometric quality of the skies, extinction coefficients, and photometric zero points were monitored by periodic observations of Landolt (1983) standard stars (typically 10–15 observations per night). The majority of the standard stars were selected to have broadband $V-R_c$ and $B-V$ colors similar to those of BCGs. However, some bluer stars were also observed in order to evaluate the significance of second-order extinction terms—these turned out to be unimportant. The quality of the atmospheric extinction transformations in R_c was always excellent, with the rms deviations of the standard stars from the mean extinction line being always less than 0.01 mag on photometric nights.

As a variety of CCDs and filter sets were used during the course of this program, we observed a sample of 32 galaxies in common between the various runs to verify that all observations were reduced to consistent photometric zero points as well as to determine the basic accuracy of the galaxy photometry. We also used the overlap observations to verify that the relative pixel scales given in Table 2 were correct, an important consideration, given that the photometry depends on aperture size. Specifically, 25 BCGs were observed on two separate runs; five BCGs were observed on three separate runs; one BCG (A496) was observed on four separate runs; and one galaxy (the second brightest member in A548) was observed on all five runs. The apparent R_c-band metric magnitudes for galaxies with repeated observations are presented in Table 4. The rms scatter for the R_c-band galaxy photometry at the adopted metric aperture (see below) is 0.020 mag, which implies a random error of 0.014 mag for any given galaxy. The B-band photometry is somewhat poorer and has a random error of 0.025 mag. In principle, the repeat observations could be used to measure any zero-point offsets that might be required to correct for systematic differences between the runs. We found that such corrections were not necessary, however; the average photometry from all runs agreed to 0.01 mag without any adjustment.

We have also compared our photometry to the combined photoelectric and CCD R_c photometry of Colless et al. (1993) as an external check for the 21 galaxies that we have in common. The comparisons are presented in Table 5, where we have interpolated our own photometry to the apertures given by Colless et al. A straight comparison between the two data sets shows us to be brighter by -0.010 ± 0.012 mag with an rms difference of 0.057 mag. A few galaxies in Table 5, however, have much larger disagreements than any differences seen in Table 4. If we eliminate the two galaxies with deviations over 0.1 mag, located in A76 and A2589, then the mean offset between us and Colless et al. becomes -0.026 ± 0.007 mag,

TABLE 3

BRIGHTEST CLUSTER GALAXY APERTURE PHOTOMETRY

Abell	Rad	R_c	$B-R_c$	Abell	Rad	R_c	$B-R_c$	Abell	Rad	R_c	$B-R_c$	Abell	Rad	R_c	$B-R_c$	Abell	Rad	R_c	$B-R_c$	Abell	Rad	R_c	$B-R_c$
76	15.53	13.491	1.848		27.16	13.618	1.627		51.78	11.857	...	496	17.79	13.160	1.714		45.82	12.077	1.642		50.81	13.926	...
	19.41	13.356	1.845		33.95	13.552	1.622						22.24	12.964	1.702		57.27	11.985	1.638		63.51	13.707	...
	24.26	13.223	1.843		42.44	13.493	1.613	295	13.69	13.792	1.687		27.80	12.780	1.689		71.59	11.900	1.633				
	30.33	13.095	1.842						17.11	13.652	1.685		34.75	12.603	1.753					957	13.45	13.544	1.742
	37.91	12.974	1.844	193	12.20	14.022	1.776		21.39	13.523	1.681		43.44	12.441	1.757	576	15.15	13.982	1.750		16.81	13.359	1.738
	47.39	12.866	1.850		15.25	13.860	1.765		26.74	13.396	1.678		54.30	12.291	1.770		18.94	13.903	1.739		21.02	13.178	1.735
					19.06	13.691	1.752		33.42	13.268	1.676		67.87	12.132	1.806		23.68	13.842	1.724		26.27	13.003	1.739
119	13.21	13.711	1.729		23.83	13.524	1.735		41.78	13.143	1.675		84.84	11.937	1.918		29.60	13.799	1.704		32.84	12.841	1.745
	16.51	13.524	1.722		29.78	13.367	1.719		52.22	12.999	1.700										41.05	12.688	1.755
	20.64	13.342	1.717		37.23	13.224	1.708					533	12.76	14.042	1.660	634	21.02	13.034	1.717		51.31	12.543	1.791
	25.80	13.167	1.740					347	29.36	12.318	1.663		15.94	13.918	1.648		26.28	12.909	1.714		64.14	12.406	...
	32.25	13.006	1.737	194	31.11	12.045	1.609		36.70	12.173	1.668		19.93	13.802	1.635		32.85	12.797	1.712		80.18	12.278	...
	40.32	12.864	1.737		38.89	11.890	1.618		45.88	12.029	1.675		24.91	13.697	1.623		41.06	12.694	1.712		100.22	12.137	...
	50.40	12.772	1.713		48.61	11.752	1.631		57.35	11.893	1.689		31.14	13.603	1.609		51.32	12.594	1.712		125.27	11.977	...
	62.99	12.679	...		60.76	11.630	1.649		71.68	11.762	1.707		38.93	13.488	1.616		64.15	12.499	...		156.59	11.803	...
					75.96	11.519	1.677						48.66	13.383	1.757		80.19	12.404	...				
147	13.51	13.767	1.668		94.94	11.415	1.719	376	12.07	14.188	1.809		60.83	13.211	...					999	18.42	13.344	1.690
	16.89	13.660	1.664						15.08	14.017	1.805		76.03	13.078	...	671	11.86	13.772	1.781		23.02	13.236	1.688
	21.11	13.562	1.661	195	13.69	13.903	1.731		18.86	13.853	1.803		95.04	12.936	...		14.82	13.599	1.775		28.78	13.131	1.684
	26.39	13.474	1.660		17.11	13.786	1.725		23.57	13.698	1.802						18.53	13.427	1.772		35.97	13.024	1.681
	32.99	13.395	1.661		21.39	13.680	1.718		29.46	13.553	1.806	539	19.91	13.295	1.754		23.16	13.261	1.770		44.97	12.921	1.682
	41.24	13.324	1.664		26.73	13.584	1.710		36.83	13.414	1.816		24.89	13.171	1.743		28.95	13.103	1.771		56.21	12.823	1.695
					33.41	13.492	1.705						31.11	13.051	1.737		36.18	12.956	1.778		70.26	12.728	...
160	13.40	14.250	1.765		41.77	13.417	1.696	397	17.33	13.468	1.796		38.89	12.933	1.730		45.23	12.821	1.786				
	16.75	14.064	1.759						21.67	13.326	1.796		48.61	12.816	1.725		56.54	12.701	...	1016	18.31	13.531	1.665
	20.94	13.890	1.756	260	15.70	13.325	1.721		27.08	13.187	1.797		60.77	12.699	1.736		70.67	12.607	...		22.89	13.424	1.666
	26.18	13.734	1.753		19.62	13.181	1.717		33.85	13.049	1.803										28.61	13.323	1.667
	32.72	13.595	1.749		24.53	13.043	1.714		42.32	12.920	1.807	548	15.00	13.568	1.665	779	25.39	11.996	1.650		35.77	13.227	1.673
	40.90	13.470	1.751		30.66	12.907	1.714		52.90	12.804	1.810		18.75	13.446	1.657		31.74	11.850	1.649		44.71	13.136	1.688
					38.33	12.777	1.716						23.43	13.330	1.647		39.67	11.709	1.650		55.88	13.037	1.713
168	13.13	13.876	1.713		47.91	12.651	1.723	407	12.52	14.495	1.890		29.29	13.220	1.632		49.59	11.572	1.655		69.85	12.930	...
	16.42	13.733	1.711						15.65	14.280	1.902		36.61	13.110	1.687		61.99	11.438	1.659				
	20.52	13.601	1.709	261	12.72	13.918	1.695		19.56	14.088	1.916		45.77	13.036	1.655		77.48	11.311	1.657	1060	48.91	11.340	1.675
	25.65	13.478	1.708		15.89	13.778	1.693		24.45	13.894	1.933		57.21	12.900	1.686		96.86	11.193	...		61.14	11.139	1.668
	32.06	13.364	1.708		19.87	13.646	1.691		30.56	13.702	1.944		71.51	12.778	...						76.43	10.954	1.660
	40.08	13.259	1.712		24.84	13.521	1.693						89.39	12.664	...	912	13.32	14.409	1.702		95.54	10.773	1.653
	50.10	13.200	1.690		31.04	13.405	1.701	419	14.48	14.320	1.615		111.74	12.543	...		16.65	14.304	1.696		119.42	10.586	1.652
	62.63	13.139	1.686		38.81	13.295	1.718		18.11	14.238	1.614		139.67	12.421	...		20.81	14.209	1.696		149.28	10.412	1.653
									22.63	14.162	1.615						26.01	14.123	1.701		186.60	10.257	...
189	17.38	13.778	1.634	262	33.14	12.251	1.710		28.29	14.093	1.620	569	29.32	12.304	1.648		32.52	14.046	1.752				
	21.73	13.694	1.631		41.43	12.055	1.708		35.36	14.041	1.635		36.65	12.181	1.644		40.65	13.986	...	1100	12.86	14.034	1.709

TABLE 3—*Continued*

Abell	Rad	R_c	$B-R_c$	Abell	Rad	R_c	$B-R_c$	Abell	Rad	R_c	$B-R_c$	Abell	Rad	R_c	$B-R_c$	Abell	Rad	R_c	$B-R_c$	Abell	Rad	R_c	$B-R_c$
	16.07	13.895	1.703	1213	12.77	13.951	1.674		27.60	12.873	1.661		60.40	11.316	...		20.74	13.124	1.689		24.57	13.227	...
	20.09	13.766	1.700		15.97	13.821	1.666		34.50	12.727	1.654		75.50	11.196	...		25.93	12.915	1.683		30.71	13.061	...
	25.11	13.645	1.700		19.96	13.709	1.657		43.12	12.583	1.648		94.37	11.086	...		32.41	12.721	1.673		38.39	12.913	...
	31.39	13.530	1.700		24.95	13.618	1.651		53.90	12.440	1.639						40.51	12.538	1.666		47.99	12.782	...
	39.23	13.423	1.697		31.19	13.539	1.646		67.38	12.295	1.626	1736	13.32	13.357	1.783		50.64	12.367	1.666		59.99	12.666	...
	49.04	13.322	1.695		38.99	13.458	1.636		84.22	12.148	1.605		16.65	13.209	1.780		63.30	12.205	...		74.98	12.573	...
					48.73	13.373	1.624						20.81	13.076	1.778		79.12	12.050	...		93.73	12.487	...
1139	15.20	13.751	1.738					1367	26.84	12.149	1.624		26.02	12.952	1.771								
	19.00	13.608	1.741	1228	16.05	13.717	1.636		33.56	12.011	1.621		32.52	12.833	1.761	2063	16.49	13.522	1.659	2152	13.05	13.943	1.657
	23.75	13.472	1.746		20.07	13.610	1.632		41.95	11.893	1.616		40.65	12.714	1.755		20.61	13.321	1.650		16.32	13.846	1.633
	29.69	13.339	1.755		25.08	13.509	1.625		52.43	11.784	1.612		50.81	12.597	...		25.77	13.140	1.641		20.40	13.760	1.588
	37.11	13.207	1.770		31.35	13.415	1.620		65.54	11.680	1.609		63.51	12.496	...		32.21	12.977	1.631		25.50	13.684	1.504
	46.39	13.083	1.798		39.19	13.326	1.615		81.92	11.586	1.605		79.39	12.422	...		40.26	12.829	1.613		31.87	13.617	...
	57.99	12.961	1.848		48.99	13.241	1.617		102.41	11.513	...						50.32	12.691	...		39.84	13.560	...
												1836	16.12	13.291	1.726		62.91	12.558	...		49.80	13.505	...
1142	16.91	13.463	1.663	1257	17.03	13.890	1.625	1631	12.91	13.841	1.724		20.15	13.144	1.710		78.63	12.425	...		62.25	13.469	...
	21.14	13.332	1.657		21.29	13.826	1.612		16.14	13.677	1.717		25.19	13.009	1.689		98.29	12.320	...		77.81	13.448	...
	26.43	13.199	1.653		26.62	13.774	1.596		20.17	13.527	1.710		31.49	12.891	1.663								
	33.03	13.062	1.647		33.27	13.727	1.575		25.22	13.390	1.696		39.36	12.787	1.628	2107	14.11	13.478	1.756	2162	17.90	13.038	...
	41.29	12.925	1.645		41.59	13.681	1.543		31.52	13.262	1.678		49.20	12.692	1.588		17.64	13.286	1.750		22.37	12.916	...
	51.62	12.801	1.643						39.40	13.140	...		61.50	12.602	...		22.05	13.106	1.739		27.97	12.794	...
	64.52	12.699	1.645	1267	17.87	13.472	1.631		49.25	13.025	...		76.87	12.516	...		27.56	12.939	1.725		34.96	12.677	...
					22.34	13.386	1.627		61.56	12.914	...						34.45	12.787	1.710		43.70	12.565	...
1177	18.42	13.132	1.647		27.92	13.318	1.626					1983	13.09	14.005	1.733		43.07	12.645	1.691		54.62	12.464	...
	23.03	12.954	1.643		34.90	13.258	...	1644	12.75	13.887	1.792		16.36	13.916	1.723		53.83	12.513	1.662		68.28	12.371	...
	28.78	12.783	1.635		43.63	13.196	...		15.94	13.642	1.785		20.45	13.842	1.709		67.29	12.392	1.631		85.35	12.276	...
	35.98	12.623	1.628		54.53	13.129	...		19.92	13.412	1.780		25.56	13.781	1.689								
	44.98	12.474	1.621						24.91	13.203	1.771		31.95	13.735	1.666	2147	16.58	13.475	1.713	2197	18.89	12.486	...
	56.22	12.331	1.614	1308	11.76	13.922	1.743		31.13	13.013	1.761		39.94	13.702	1.637		20.72	13.306	1.711		23.62	12.341	...
	70.27	12.191	...		14.70	13.788	1.734		38.92	12.840	1.755		49.93	13.686	1.598		25.90	13.154	1.707		29.52	12.200	...
	87.84	12.057	...		18.37	13.654	1.725		48.64	12.682	1.751						32.38	13.014	1.703		36.90	12.069	...
	109.80	11.927	...		22.97	13.522	1.716		60.81	12.537	...	2040	13.04	14.295	1.743		40.48	12.874	1.697		46.13	11.953	...
					28.71	13.398	1.702		76.01	12.397	...		16.29	14.126	1.725		50.60	12.731	1.692		57.66	11.847	...
1185	17.71	13.210	1.594		35.89	13.288	1.683		95.01	12.261	...		20.37	13.938	1.712		63.24	12.582	1.695		72.08	11.739	...
	22.14	13.049	1.598		44.86	13.192	...		118.76	12.110	...		25.46	13.741	1.697		79.06	12.361	...		90.10	11.637	...
	27.68	12.916	...		56.08	13.107	...		148.45	11.948	...		31.82	13.550	1.677		98.82	12.169	...		112.62	11.543	...
	34.60	12.795	...		70.09	13.019	...						39.78	13.387	1.663		123.52	11.951	...				
	43.24	12.679	...		87.62	12.940	...	1656	24.74	11.863	1.638		49.73	13.264	1.657		154.41	11.704	...	2199	18.92	12.777	...
	54.06	12.566	...						30.92	11.712	1.632		62.16	13.171	...						23.65	12.582	...
	67.57	12.452	...	1314	17.66	13.155	1.674		38.66	11.572	1.618					2151	15.72	13.591	...		29.56	12.401	...
					22.08	13.015	1.668		48.32	11.441	...	2052	16.59	13.346	1.696		19.66	13.406	...		36.95	12.234	...

TABLE 3—*Continued*

Abell	Rad	R_c	$B-R_c$	Abell	Rad	R_c	$B-R_c$	Abell	Rad	R_c	$B-R_c$	Abell	Rad	R_c	$B-R_c$	Abell	Rad	R_c	$B-R_c$	Abell	Rad	R_c	$B-R_c$
	46.18	12.076	···	2657	14.38	14.219	···		73.28	11.750	···		16.75	14.242	1.658		47.27	13.244	···		82.25	12.789	···
	57.73	11.927	···		17.98	14.129	···						20.94	14.154	1.668								
	72.16	11.784	···		22.47	14.053	···	2877	23.76	11.771	1.640		26.18	14.073	1.682	3526	52.60	10.590	1.726	3537	35.24	11.666	1.707
	90.20	11.648	···		28.09	13.991	···		29.70	11.622	1.638		32.72	13.994	1.703		65.75	10.408	1.713		44.05	11.540	1.704
	112.75	11.523	···		35.11	13.935	···		37.12	11.480	1.638		40.90	13.914	1.731		82.18	10.241	1.699		55.06	11.421	1.703
									46.40	11.342	1.640						102.73	10.092	1.681		68.82	11.311	1.704
2247	14.88	13.860	···	2666	20.82	12.559	1.623		58.01	11.214	1.644	3374	12.66	14.409	1.611		128.41	9.962	1.662		86.03	11.204	1.708
	18.60	13.756	···		26.02	12.421	1.620		72.51	11.097	···		15.82	14.334	1.614		160.51	9.847	1.638		107.53	11.096	1.717
	23.25	13.662	···		32.53	12.295	1.619						19.77	14.288	1.621						134.42	10.981	1.736
	29.06	13.582	···		40.66	12.187	1.622	2881	13.31	14.389	1.626		24.72	14.255	1.630	3528	11.24	14.009	···		168.02	10.886	···
	36.33	13.510	···		50.82	12.094	1.627		16.63	14.287	1.624		30.90	14.226	1.626		14.05	13.847	···				
	45.41	13.435	···		63.53	12.010	1.637		20.79	14.199	1.628		38.62	14.205	···		17.57	13.686	···	3542	17.23	13.757	···
	56.77	13.358	···						25.99	14.124	1.629						21.96	13.530	···		21.54	13.687	···
				2717	12.16	14.283	1.680					3376	13.04	13.846	1.736		27.45	13.383	···		26.93	13.625	···
2572	14.00	13.662	1.868		15.20	14.065	1.658	2896	18.31	13.368	1.623		16.30	13.695	1.727		34.31	13.245	···		33.66	13.566	···
	17.50	13.536	1.871		19.00	13.842	1.631		22.88	13.279	1.621		20.37	13.552	1.718		42.89	13.109	···		42.08	13.509	···
	21.88	13.403	1.862		23.75	13.620	1.600		28.60	13.199	1.624		25.46	13.416	1.710		53.61	12.967	···		52.59	13.449	···
	27.35	13.260	1.846		29.69	13.411	1.559		35.75	13.126	1.632		31.83	13.286	1.705		67.01	12.811	···		65.74	13.377	···
	34.19	13.107	1.821		37.11	13.221	···		44.69	13.060	1.649		39.79	13.170	1.736		83.77	12.641	···				
	42.73	12.956	1.810		46.39	13.046	···						49.73	13.069	1.696		104.71	12.454	···	3553	12.59	14.614	···
					57.99	12.882	···	2911	28.40	12.872	1.636		62.17	12.978	···		130.89	12.250	···		15.74	14.504	···
2589	14.03	13.844	1.587						35.50	12.788	1.636										19.68	14.410	···
	17.54	13.653	1.587	2731	18.60	13.049	1.660		44.38	12.719	1.641	3381	15.64	13.997	1.693	3530	11.32	14.107	···		24.60	14.324	···
	21.93	13.466	1.586		23.25	12.914	1.663		55.47	12.665	1.654		19.55	13.849	1.705		14.14	13.924	···		30.75	14.246	···
	27.41	13.286	1.589		29.07	12.781	1.670						24.44	13.710	1.726		17.68	13.739	···		38.43	14.183	···
	34.26	13.118	1.589		36.33	12.653	1.684	3144	13.32	14.200	1.666		30.55	13.578	1.765		22.10	13.551	···		48.04	14.141	···
	42.83	12.966	1.584		45.42	12.536	1.707		16.65	14.089	1.666		38.18	13.448	1.818		27.63	13.364	···		60.05	14.120	···
					56.77	12.431	1.723		20.81	13.985	1.669		47.73	13.231	···		34.53	13.187	···		75.07	14.115	···
2593	13.95	13.833	1.689						26.01	13.888	1.676		59.66	13.095	···		43.17	13.029	···				
	17.43	13.626	1.687	2806	21.22	12.870	1.644		32.52	13.797	1.691						53.96	12.884	···	3554	12.68	14.198	2.069
	21.79	13.445	1.683		26.52	12.766	1.657		40.65	13.721	1.720	3389	21.96	12.620	1.657		67.45	12.740	···		15.85	14.020	2.145
	27.24	13.286	1.681		33.15	12.678	1.678		50.81	13.659	···		27.45	12.492	1.654						19.81	13.858	2.226
	34.05	13.147	1.687		41.44	12.600	1.713						34.32	12.375	1.678	3532	11.04	14.330	···		24.77	13.709	2.311
					51.80	12.526	1.757	3193	17.20	13.351	1.624		42.89	12.273	1.704		13.80	14.154	···		30.96	13.564	2.379
2634	18.50	12.902	1.713		64.75	12.458	···		21.50	13.228	1.612						17.25	13.980	···		38.70	13.424	2.383
	23.12	12.741	1.710						26.87	13.118	1.599	3395	12.39	14.276	1.841		21.56	13.803	···		48.37	13.302	2.425
	28.91	12.586	1.710	2870	24.01	12.424	1.580		33.59	13.015	1.583		15.49	14.079	1.829		26.95	13.621	···		60.47	13.193	···
	36.13	12.433	1.712		30.02	12.269	1.575		41.98	12.917	1.640		19.36	13.896	1.823		33.69	13.436	···		75.58	13.091	···
	45.16	12.284	1.720		37.52	12.122	1.570		52.48	12.845	1.649		24.20	13.720	1.821		42.11	13.261	···				
	56.46	12.139	1.731		46.90	11.988	1.566						30.26	13.552	1.826		52.64	13.093	···	3556	12.54	13.617	1.758
					58.62	11.870	1.578	3367	13.40	14.343	1.653		37.82	13.393	1.840		65.80	12.934	···		15.67	13.474	1.748

TABLE 3—*Continued*

Abell	Rad	R_c	$B-R_c$	Abell	Rad	R_c	$B-R_c$	Abell	Rad	R_c	$B-R_c$	Abell	Rad	R_c	$B-R_c$	Abell	Rad	R_c	$B-R_c$	Abell	Rad	R_c	$B-R_c$
	19.59	13.341	1.737		47.18	13.069	1.660		23.56	12.823	1.722		125.73	11.548	···		40.67	13.056	1.673		29.68	12.971	1.658
	24.49	13.214	1.720		58.98	12.902	···		29.45	12.592	1.713		157.16	11.367	···		50.84	12.941	1.692		37.10	12.873	1.685
	30.61	13.095	1.701		73.72	12.736	···		36.82	12.392	1.700						63.55	12.847	···		46.37	12.784	1.684
	38.27	12.990	1.681		92.16	12.570	···		46.02	12.218	1.680	3656	29.60	11.919	1.620		79.44	12.739	···		57.97	12.639	···
	47.83	12.907	1.664		115.19	12.401	···		57.53	12.062	1.658		37.00	11.771	1.606		99.30	12.624	···				
	59.79	12.838	···		143.99	12.233	···		71.91	11.913	1.634		46.25	11.621	1.589					3869	14.80	13.699	1.673
									89.88	11.762	···		57.81	11.471	1.572	3733	15.84	14.005	1.871		18.51	13.604	1.671
3558	12.69	13.562	1.752	3564	12.36	14.231	1.717		112.35	11.605	···		72.26	11.327	1.560		19.80	13.850	1.875		23.13	13.517	1.670
	15.86	13.339	1.739		15.46	14.118	1.709		140.44	11.436	···		90.32	11.179	···		24.75	13.695	1.889		28.91	13.438	1.677
	19.83	13.130	1.726		19.32	14.020	1.697		175.55	11.252	···		112.91	11.025	···		30.93	13.546	1.921		36.14	13.371	1.688
	24.79	12.937	1.714		24.15	13.936	1.682						141.13	10.865	···		38.67	13.412	1.919		45.18	13.317	1.708
	30.98	12.754	1.702		30.19	13.870	1.659	3572	14.81	13.795	1.698		176.42	10.557	···		48.33	13.296	···		56.47	13.270	1.733
	38.73	12.585	1.688		37.73	13.826	1.627		18.51	13.707	1.680						60.41	13.192	···				
	48.41	12.429	1.665		47.17	13.798	1.584		23.14	13.627	1.658	3676	14.61	13.623	1.576					4038	20.27	12.980	1.593
	60.51	12.283	1.639		58.96	13.780	1.532		28.93	13.557	1.631		18.27	13.504	1.564	3736	12.29	13.600	1.711		25.34	12.867	1.582
	75.64	12.144	1.606						36.16	13.498	1.599		22.83	13.394	1.557		15.36	13.429	1.708		31.67	12.763	1.574
	94.55	12.014	···	3565	46.64	10.871	1.449		45.20	13.444	1.550		28.54	13.299	1.548		19.20	13.271	1.705		39.59	12.669	1.570
	118.19	11.883	···		58.30	10.740	1.446		56.50	13.392	1.491		35.68	13.221	1.538		24.00	13.125	1.702		49.49	12.590	1.566
					72.87	10.614	1.442						44.59	13.169	1.527		30.01	12.992	1.699		61.86	12.530	1.572
3559	12.77	13.628	1.779		91.09	10.490	1.438	3574	38.03	11.470	1.642						37.51	12.872	1.698				
	15.96	13.477	1.782		113.86	10.370	1.435		47.54	11.289	1.631	3677	12.92	14.498	1.748		46.88	12.765	1.696	4049	20.25	12.826	1.625
	19.95	13.326	1.789		142.33	10.247	···		59.43	11.110	1.621		16.15	14.398	1.738		58.61	12.667	1.696		25.31	12.700	1.629
	24.94	13.182	1.797						74.28	10.944	1.608		20.19	14.298	1.727		73.26	12.577	1.710		31.64	12.577	1.636
	31.17	13.048	1.805	3566	12.52	14.383	···		92.85	10.799	1.589		25.24	14.196	1.712						39.55	12.450	···
	38.97	12.920	1.816		15.64	14.289	···		116.07	10.664	1.569		31.55	14.088	1.698	3742	35.28	12.046	1.597		49.44	12.322	···
	48.71	12.811	1.836		19.56	14.208	···		145.08	10.529	1.544		39.43	13.972	1.684		44.10	11.942	1.592		61.80	12.199	···
	60.89	12.716	1.876		24.44	14.142	···		181.35	10.399	···		49.29	13.831	1.709		55.12	11.841	1.590				
	76.11	12.617	1.949		30.55	14.080	···										68.90	11.746	1.590	4059	12.17	13.716	1.728
	95.13	12.511	···		38.19	14.017	···	3575	16.00	14.423	1.633	3698	27.96	12.512	1.687						15.22	13.496	1.723
					47.74	13.955	···		20.01	14.354	1.597		34.96	12.420	1.687	3744	15.67	13.478	1.798		19.02	13.287	1.721
3560	47.96	11.465	1.603						25.01	14.285	1.541		43.69	12.332	1.688		19.59	13.375	1.805		23.77	13.096	1.717
	59.94	11.384	1.602	3570	16.07	13.751	···		31.26	14.215	1.454		54.62	12.248	1.690		24.48	13.274	1.818		29.72	12.920	1.717
	74.93	11.307	1.601		20.09	13.668	···		39.07	14.142	···						30.60	13.181	1.851		37.15	12.761	1.719
	93.66	11.227	···		25.11	13.594	···					3716	13.33	13.833	1.688		38.25	13.097	1.901		46.43	12.619	1.728
					31.39	13.533	···	3581	26.37	12.617	1.690		16.66	13.657	1.682		47.82	13.012	1.977		58.04	12.485	1.755
3562	12.37	14.056	1.763		39.23	13.488	···		32.96	12.465	1.681		20.82	13.489	1.676						72.55	12.349	1.807
	15.46	13.883	1.752		49.04	13.460	···		41.20	12.320	1.678		26.03	13.329	1.672	3747	18.99	13.189	1.635				
	19.33	13.716	1.739		61.30	13.448	···		51.50	12.183	1.678		32.54	13.185	1.669		23.74	13.075	1.642				
	24.16	13.550	1.724						64.37	12.052	1.678												
	30.20	13.387	1.705	3571	15.08	13.356	1.736		80.46	11.922	1.687												
	37.75	13.228	1.683		18.85	13.079	1.730		100.58	11.784	···												

TABLE 4

INTERRUN PHOTOMETRY COMPARISONS

Abell	Run 1	Run 2	Run 3	Run 4	Run 5
119-1.....	...	13.528	13.521	...	...
168-1.....	...	13.734	13.732	...	...
195-1.....	...	13.809	13.763	...	...
295-1.....	...	13.681	13.622	...	...
496-1.....	12.952	12.981	12.968	12.955	...
533-1.....	...	13.936	13.944	...	13.897
539-1.....	...	13.194	13.139	13.180	...
548-1.....	13.418	13.467	...	...	13.449
548-2.....	13.485	13.470	13.472	13.455	13.492
569-1.....	...	12.171	...	12.186	...
912-1.....	...	...	14.312	14.313	14.296
957-1.....	...	...	13.344	13.369	13.361
1631-2.....	...	...	...	11.691	11.695
1644-1.....	...	...	...	13.644	13.640
1836-1.....	...	...	...	13.141	13.146
2063-1.....	...	...	...	13.317	13.325
2147-1.....	...	...	...	13.327	13.285
2152-1.....	...	...	...	13.825	13.868
2657-2.....	...	14.217	...	14.186	...
2870-1.....	12.286	...	12.253	...	...
2881-2.....	14.314	14.295	...	...	...
2911-2.....	12.773	...	12.837	...	...
3193-1.....	13.248	...	13.209	...	...
3367-1.....	...	14.259	14.226	...	...
3374-1.....	...	14.327	14.341	...	...
3376-1.....	13.684	...	13.706	...	...
3381-1.....	13.817	...	13.881	...	...
3389-1.....	12.508	...	12.476	...	...
3656-1.....	...	...	11.753	11.780	...
3716-1.....	...	...	13.647	13.668	...
3733-1.....	13.843	...	13.857	...	...
3747-1.....	13.075	...	13.074	...	...
3747-2.....	13.472	...	13.459	...	...

NOTE.—Comparisons are shown for the R_c-band photometry at the adopted metric aperture in the Local Group frame. Details of the runs are given in Table 2. A portion of the comparisons were based on the second-ranked galaxies in some clusters.

TABLE 5

EXTERNAL PHOTOMETRY COMPARISONS

Abell	Radius	R_C	R_W	$R_W - R_C$
76.....	14.95	13.379	13.511	0.132
119.....	14.95	13.595	13.604	0.009
168.....	14.95	13.801	13.790	−0.011
260.....	14.95	13.340	13.354	0.014
262.....	14.95	12.981	12.926	−0.055
496.....	14.95	13.305	13.318	0.013
548.....	14.95	13.659	13.568	−0.091
1656.....	14.95	12.272	12.239	−0.033
1983.....	19.75	13.931	13.853	−0.078
2040.....	14.95	14.217	14.193	−0.024
2052.....	14.95	13.483	13.456	−0.027
2107.....	14.95	13.448	13.427	−0.021
2147.....	19.75	13.384	13.340	−0.044
2151.....	14.95	13.663	13.633	−0.030
2162.....	19.75	13.030	12.984	−0.046
2197.....	19.75	12.483	12.457	−0.026
2247.....	14.95	13.895	13.858	−0.037
2589.....	14.95	13.637	13.784	0.147
2593.....	14.95	13.740	13.760	0.020
2666.....	9.60	13.107	13.097	−0.010
2657.....	14.95	14.214	14.202	−0.012

NOTE.—Comparisons are shown for the R_c-band photoelectric photometry of Colless et al. 1993 (R_C) and the present work (R_W), for the selected Colless et al. aperture.

with an rms difference of 0.030 mag per galaxy, which nicely matches the quadrature sum of the Colless et al. stated internal error of 0.025 mag, and our own of 0.014 mag. In either case, however, the comparison with Colless et al. suggests that there may be a slight zero-point mismatch between the two sets. We have emphasized internal consistency in our photometry, but have invested much less effort in tying our observations to the true photoelectric R_c system. We thus present our photometry with the caveat that it may contain a slight offset from other external sets of R_c galaxy observations.

3.2. *Redshifts*

The majority of the redshift data used here are obtained from the literature. However, new redshifts were obtained for 33 ACO clusters (and their BCGs) by us at CTIO and for 17 northern BCGs by J. Huchra (1992) and A. Zabludoff (1992) at the Multiple Mirror Telescope (MMT). For the southern clusters, we used the CTIO 1.5 m telescope and the GEC-CCD spectrograph with grating No. 09 (8.4 Å resolution) over the spectral range 3900–6300 Å. Redshifts were determined primarily from the Mg I and Na D absorption lines using the Tonry-Davis (Tonry & Davis 1979) cross-correlation technique. The galaxies NGC 1316, NGC 1427, NGC 3115, NGC 6868, and NGC 7507 were used as templates. The typical error for the CTIO redshifts is 60 km s^{-1}. A similar reduction procedure was used on the MMT spectrograph data. The MMT redshifts have a typical uncertainty of 30 km s^{-1}. We also observed 10 galaxies (from CTIO) for which independent redshift data already exist to estimate any systematic errors. We find a typical scatter of ± 60 km s^{-1} between our CTIO redshifts and the published values, consistent with expectations based on the internal errors. There is no significant velocity offset. Table 6 presents all the new heliocentric redshifts obtained during the course of our survey and, therefore, includes galaxies which have $z > 0.05$ as well. We note that the new BCG redshift data are also included in Table 6; thus there is some redundancy with Table 1. The source codes in Table 6 for data obtained by us at CTIO are "2" and "3"; source code "1" refers to data obtained by Huchra and Zabludoff at the MMT.

At the minimum, we have velocities for at least four galaxies per cluster including the BCG, and 51% of the clusters have measurements for 10 or more member galaxies. Fortunately, BCGs are generally close to the kinematic centers of the clusters (Quintana & Lawrie 1982; Zabludoff, Huchra, & Geller 1990; Zabludoff et al. 1993), so even where we have few velocities, because we include the BCGs, the error in the mean cluster redshifts is small. BCGs, in general, are not at rest with respect to their cluster, but deviate from the mean velocity with a typical dispersion of σ_1, which can be compared to the typically larger one-dimensional velocity dispersion for all cluster members, σ_C. For the 42 clusters with more than 20 members, we find $\sigma_C = 666$ km s^{-1}, in excellent agreement with Zabludoff et al. (1990). For the same clusters, we find $\sigma_1 = 264$ km s^{-1} after correcting for the typical error in the mean cluster redshift of 102 km s^{-1}. The distribution of BCG-cluster velocity differences appears to be Gaussian, so we argue that clusters with "significant" BCG peculiar velocities simply represent the more extreme examples of a general phenomenon. From these results we conclude that we should give the BCGs a weight of $(\sigma_C/\sigma_1)^2 \approx 6.0$ compared to other cluster members when calculating mean cluster redshifts.

TABLE 6

GALAXY REDSHIFT OBSERVATIONS

Abell	R.A. (J2000)	Decl.	cz[a]	σ	Source	Notes
147-G1	01^{h}08^{m}37^s.90	+02°16′06″.1	13138	33	1	
260-GA	01 50 42.96	+33 04 54.8	10699	28	1	
GB	01 51 23.57	+33 01 51.9	10411	26	1	
295-G1	02 02 17.24	−01 07 40.6	12818	29	1	
G2	02 02 20.17	−01 06 37.2	12996	31	1	
419-G1	03 08 15.84	−23 41 29.0	20391	34	1	1
484-G1	04 16 23.19	−07 40 59.0	20914	42	1	2
G2	04 16 47.68	−07 40 32.3	20714	31	1	2
533-G2	05 01 35.99	−22 36 03.1	14642	34	1	
912-G6	10 01 10.83	−00 03 46.8	27828	84	2	1
1100-G1	10 48 45.73	+22 13 03.4	13990	45	1	
1139-G1	10 58 11.02	+01 36 15.4	11460	170	1	
1644-G1	12 57 11.76	−17 24 35.0	14237	42	1	
G2	12 57 49.30	−17 32 44.5	14013	50	1	
1837-G1	14 01 36.37	−11 07 44.0	20722	3	1	2
2040-G1	15 12 47.74	+07 26 02.0	13680	30	1	
2107-G1	15 39 39.05	+21 46 55.7	12613	31	1	
2148-G1	16 03 19.79	+25 27 14.3	26606	82	1	2
2806-G1	00 40 12.92	−56 09 15.0	8244	49	3	
G3	00 40 03.53	−56 10 53.3	8478	48	3	
2860-G1	01 04 03.85	−39 46 59.2	32224	63	3	2
2870-G2	01 07 44.43	−46 51 48.6	7571	39	3	
G3	01 07 14.69	−46 50 20.6	9317	46	3	
2882-G1	01 11 22.08	−17 04 16.7	13661	32	1	Spiral
G2	01 10 54.46	−17 11 51.6	12665	38	1	
G3	01 11 14.14	−17 04 14.5	13363	43	1	
2933-G1	01 40 59.38	−54 37 27.8	27894	57	3	2
G2	01 40 35.13	−54 30 52.8	27355	65	3	2
2995-G3	02 14 55.44	−24 51 18.3	11050	56	3	
3202-G1	04 01 00.55	−53 41 08.6	21133	52	3	2
G2	03 59 29.13	−53 38 22.6	21063	75	3	2
3367-G1	05 49 41.71	−24 32 43.7	13461	34	1	
G2	05 48 50.27	−24 21 06.3	19984	31	1	1
3374-G1	05 56 42.97	−21 15 12.4	14201	71	1	
3381-G1	06 09 53.76	−33 35 34.1	11488	57	3	
G2	06 09 48.68	−33 35 51.4	11310	56	3	
3389-G1	06 22 21.30	−64 56 04.6	8294	48	3	
G2	06 21 26.41	−64 59 37.1	8027	44	3	
G3	06 21 24.42	−64 57 45.4	8391	45	3	
3528-G1	12 54 22.31	−29 00 45.9	16425	78	2	
G4	12 54 24.91	−28 58 24.6	14754	102	2	
3537-G3	13 01 28.49	−32 20 03.2	4949	39	2	
G4	13 01 25.84	−32 31 08.5	25647	79	2	1
3545-G1	13 11 21.65	−34 04 48.2	29172	73	2	2
G3	13 11 14.52	−34 05 36.1	15029	93	2	2
3554-G1	13 19 31.53	−33 29 19.7	14333	78	2	
G4	13 19 19.76	−33 28 06.0	14605	82	2	
3557-G1	13 24 55.16	−28 53 15.8	23405	61	2	2
3570-G1	13 46 47.33	−37 54 28.4	11237	74	2	
G2	13 46 24.00	−37 58 15.5	11377	61	2	
G4	13 46 47.15	−37 54 41.9	11310	86	2	
3577-G1	13 54 14.83	−27 50 51.8	14848	83	2	
3581-G1	14 07 29.51	−27 01 07.0	6618	39	2	I4374
G2	14 07 44.13	−27 04 58.8	6595	41	2	
3653-G1	19 53 02.85	−52 02 14.8	32717	97	3	2
3656-G1	20 00 49.97	−38 34 35.9	4965	34	3	I4374
G3	20 00 09.79	−38 30 59.5	5487	39	3	
G4	20 00 25.38	−38 27 55.6	5888	34	3	
G5	20 00 00.33	−38 30 17.9	5902	32	3	
3664-G1	20 13 59.00	−80 39 08.7	41166	117	3	2
3676-GB	20 24 19.70	−40 21 39.2	12372	56	3	
3677-G1	20 26 23.56	−33 21 03.5	13787	60	3	
G2	20 26 13.18	−33 21 38.5	11930	65	3	
3695-G1	20 34 45.40	−35 49 25.9	26851	86	3	2
3698-G1	20 35 56.21	−25 16 45.3	5799	35	3	NGC 6936
G2	20 36 22.07	−25 20 30.1	5732	57	3	
G3	20 36 07.13	−25 11 54.1	6456	64	3	
3706-G1	20 42 14.56	−38 19 57.2	30763	66	3	2
3733-G1	21 01 59.07	−28 03 34.5	10943	70	3	
G3	21 02 23.82	−28 10 18.2	10816	50	3	Emission lines
G4	21 01 36.54	−28 03 33.3	12193	64	3	
3742-G1	21 06 47.32	−47 11 15.4	5163	30	3	

TABLE 6—*Continued*

Abell	R.A. (J2000)	Decl.	cz[a]	σ	Source	Notes
3744-G1	21 07 16.19	−25 28 08.4	11041	56	3	
G2	21 07 20.93	−25 29 15.3	12780	135	3	
G3	21 07 19.80	−25 29 17.1	10364	69	3	
G4	21 07 24.96	−25 25 46.8	11628	63	3	
G5	21 07 25.95	−25 25 48.5	11456	60	3	
3747-G2	21 08 28.99	−43 29 24.5	5086	30	3	
G4	21 08 41.23	−43 30 41.1	8967	49	3	
3816-G1	21 50 16.38	−55 16 35.5	11681	50	3	Emission lines
G2	21 50 44.25	−55 14 55.1	11906	69	3	
G3	21 49 58.70	−55 15 56.0	20234	54	3	1
3869-G1	22 20 45.73	−55 06 08.9	11920	61	3	
GW	22 20 45.14	−55 06 08.9	12407	75	3	
3879-G1	22 27 48.85	−69 01 24.1	19956	52	3	2
3911-G2	22 46 15.76	−52 43 42.0	29198	64	3	2

NOTES.—(1) This galaxy is a background object. (2) This galaxy is in a cluster beyond the 15,000 km s^{-1} heliocentric velocity limit. The redshift measurement, however, was obtained by us to better determine the membership of the $z \leq 0.05$ cluster sample.

[a] All velocities are heliocentric and are given in km s^{-1}.

SOURCES.—(1) MMT, J. Huchra & A. Zabludoff, private communication. (2) CTIO 1.5 m, 1991 Spring (3) CTIO 1.5 m, 1990 Fall.

A separate problem in calculating cluster redshifts is to identify the galaxies properly belonging to the cluster. Our approach is to first select candidate cluster members as those galaxies projected to be within the cylinder 1.5 h^{-1} Mpc in radius and ± 3000 km s^{-1} in depth centered on the BCG location, and then to reject outliers by demanding that the velocity distribution be Gaussian. The rejection process is allowed to proceed until the probability that the resultant distribution is Gaussian exceeds 15%. The redshift error for any given cluster will always be 264 km s^{-1} (σ_1) or less depending how many cluster members contribute to the average. The mean error in the mean cluster redshift for the entire sample is 184 km s^{-1}.

4. THE BCG DISTANCE INDICATOR

4.1. *The Luminosity-α Relationship*

As we have discussed in the introduction, the BCG distance indicator works by using

$$\alpha \equiv d \log L_m / d \log r|_{r_m} .$$

to predict L_m, where L_m is the total BCG luminosity within the circular aperture of physical radius r_m centered on the BCG nucleus. Effective use of the L_m-α relationship depends on two issues that we consider in this section, namely, (1) determination of the best relationship between L_m and α, and (2) selection of the best value of r_m. For convenience we calculate L_m using $H_0 = 80$ km s^{-1} Mpc^{-1}. This choice is motivated by analysis of secondary distance indicators applied to the Virgo Cluster BCG, NGC 4472 (Lauer & Postman 1992), although the present analysis and our results are independent of the value adopted for H_0. We have adopted the appropriate frame as that having the Abell clusters at rest on average (the *F* solution of Paper I). We have applied *K*-corrections which were computed by convolving the CCD + filter response with the spectral energy distribution of a typical BCG (Whitford 1971) converted to photons. For the *B* and R_c filters, the following analytic expressions provide excellent estimates for $z \leq 0.50$:

$$K_R = 2.5 \log_{10} (1 + 0.96z) ,$$

$$K_B = 2.5 \log_{10} (1 + 4.00z + 22.4z^2) .$$

The nominal corrections for Galactic extinction for the *B* and R_c filters are

$$A_R = 2.35E(B-V) ,$$

$$A_B = 4.05E(B-V) ,$$

where $E(B-V)$ values are obtained from Burstein & Heiles (1982) and are tabulated in Paper I. Last, we calculate r_m from angle θ_m (in arcseconds) as

$$r_m = 20.07\, h^{-1}\theta_m[1 - (1+z)^{-1/2}]/(1+z) \text{ kpc} , \quad (1)$$

which assumes $q_0 = 0.5$ (although this choice matters little at the low redshifts of the present sample).

The relationship between L_m and α for our BCG sample is shown in Figure 1, using the optimal aperture of 10 h^{-1} kpc adopted below (the data plotted are published in Paper I). The relationship looks qualitatively similar to that of Hoessel

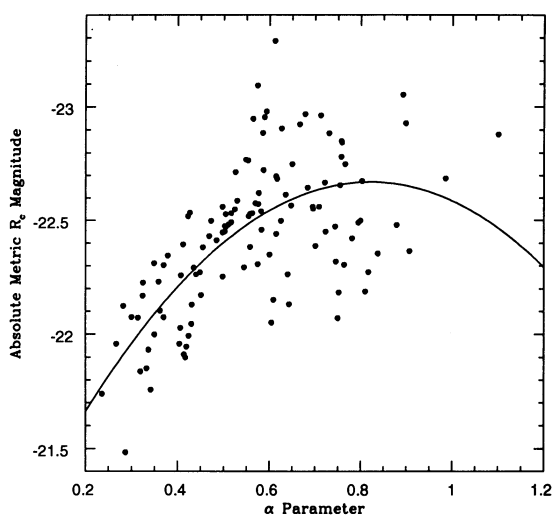

FIG. 1.—BCG R_c absolute metric luminosities are shown as a function of α, the logarithmic slope of the surface brightness profile evaluated at the metric radius. $H_0 = 80$ km s^{-1} Mpc^{-1} has been assumed. The solid line shows the mean L_m-α relationship. The relationship is shown after correction for the motion of the Local Group with respect to the Abell cluster inertial frame.

(1980). For small α the relationship appears to have a constant linear slope, but it flattens out toward larger α; a parabolic fit appears adequate to match this nonlinearity and produces significantly smaller residuals than does a purely linear fit. The scatter about the best-fit parabola is $\sigma_m = 0.244$ mag, as compared to the scatter in L_m alone of $\sigma_m = 0.327$ mag. The form of the L_m-α relationship for $H_0 = 80$ km s^{-1} Mpc^{-1} is

$$L_m = -20.896 - 4.397\alpha + 2.738\alpha^2 \quad (R_c \text{ band}) . \qquad (2)$$

with a total uncertainty of about 0.02 mag. Since the L_m-α relationship describes the flux of a BCG within a constant physical aperture, we can recast the relationship equally well as a predictor of surface brightness within the metric aperture. For $\alpha = 0.57$ (the mean value for this sample), the average surface brightness within r_m is $\mu_m = 20.787 R_c$ mag arcsec^{-2}.

The residuals about the mean metric luminosity for the entire sample ($n = 0$ order polynomial fit) and the residuals about the quadratic L_m-α relationship ($n = 2$) are Gaussian. Fits to a Gaussian distribution yield probabilities of 0.248 ($\chi^2_\nu = 1.35$) and 0.916 ($\chi^2_\nu = 0.24$), respectively, that the residuals are normally distributed. Further, a K-S test appropriate for comparing an observed distribution with the distribution expected for a Gaussian with the same mean and standard deviation (Press et al. 1986, pp. 472–475) shows that the residuals of the L_m-α relationship are consistent with having been drawn from a Gaussian distribution at a 26.3% confidence level (rejection of the Gaussian hypothesis would require confidence levels of 5% or less). The histograms of the residuals about the mean metric luminosity for the entire sample ($n = 0$ order polynomial fit) and the residuals about the quadratic L_m-α relationship ($n = 2$) are shown in Figure 2*a*. The cumulative distribution functions (CDFs) for the residuals about the $n = 0$ and $m = 2$ order polynomial fits to the L_m-α relationship are shown in Figure 2*b*, along with the corresponding CDFs for Gaussians with $\sigma_m = 0.244$ mag and $\sigma_m = 0.327$ mag. The aperture magnitudes alone, prior to the α-correction, are also Gaussian, but of course with larger scatter. The excellent agreement with a Gaussian distribution both before and after accounting for the L_m-α relationship argues strongly against the bimodal BCG luminosity function proposed by Bhavsar (1989). We suspect that the origin of the BCG luminosity distribution seen by Bhavsar is a combination of BCG misclassification by Hoessel and, in some cases, poor sky subtraction due to the small format of the CCD used by Hoessel. These effects can introduce a low-luminosity tail to the BCG luminosity distribution, perhaps causing it to appear bimodal.

Figure 3 shows the relative reduced χ^2 (normalized by the reduced χ^2 for the quadratic fit) and the scatter about the best-fit polynomial relation to the L_m-α relationship as functions of polynomial order, n. Goodness of fit is not significantly improved for $n > 2$. The minor reduction in χ^2_ν for $n > 2$, which does occur, appears to be due to better fitting of the few BCGs with extreme α, where the relationship is poorly defined. We are currently extending the BCG sample to higher redshifts and thus should fill in the endpoints of the relationship much more densely.

The choice of metric aperture size is driven by the following considerations: (1) the aperture should be large enough to avoid seeing effects that could affect the photometry at the 0.5% level, (2) the aperture should be small enough to minimize sky-subtraction errors and to avoid encompassing the outer regions of the BCGs which can vary dramatically in surface brightness depending on whether or not the BCG is also a cD

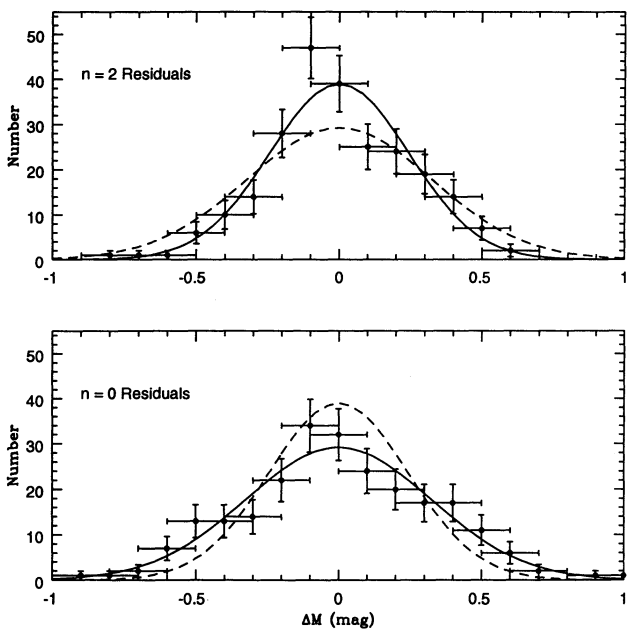

FIG. 2*a*

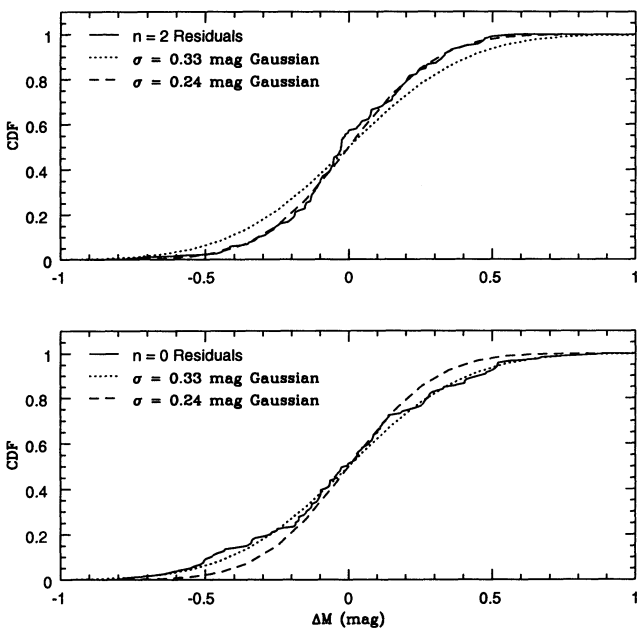

FIG. 2*b*

FIG. 2.—(*a*) Histograms of the residuals about the mean metric luminosity for the entire sample ($n = 0$) and the residuals about the quadratic L_m-α relationship ($n = 2$). The best-fit Gaussian distributions for each are superposed. (*b*) CDFs for the residuals about the mean metric luminosity for the entire sample ($n = 0$) and the residuals about the quadratic L_m-α relationship ($n = 2$). The CDFs for Gaussians with $\sigma_m = 0.244$ mag and $\sigma_m = 0.327$ mag are also shown. A K-S test between each residual CDF and the CDF for the best-fit Gaussian distribution yields a rejection of the hypothesis that the residual distributions are different from Gaussian at the 26% confidence level.

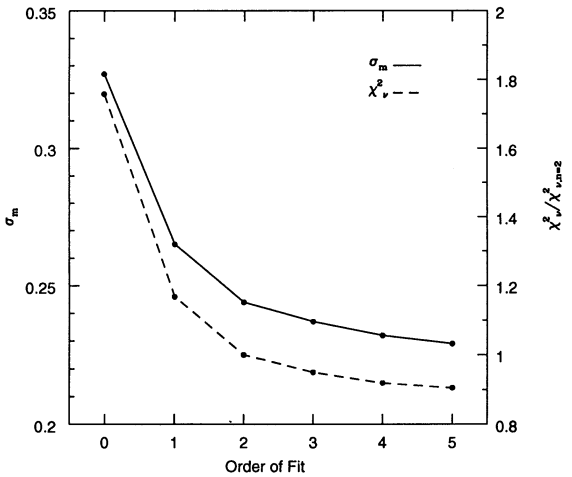

FIG. 3.—Scatter, σ_m, about the L_m-α relationship (*solid curve*) and the normalized χ^2_ν value (divided by the χ^2_ν for the quadratic fit) as functions of the polynomial order used to fit the relationship.

galaxy, and (3) within these two limits, the aperture should be selected to minimize the scatter in the BCG metric magnitudes. Figure 4 shows the scatter in the BCG metric luminosity as a function of aperture radius. The data for this plot are generated by placing apertures ranging in radius from 5 h^{-1} kpc to 20 h^{-1} kpc in intervals of 0.5 kpc on each BCG in our sample. At $z = 0.05$, this translates to an angular aperture range running from 7".50 to 30".0. The curve shows the scatter when cluster redshifts (and thus apertures) are corrected for the best-fit Local Group motion given in Paper I. The scatter is relatively constant for aperture radii less than 10 h^{-1} kpc but increases for larger radii. We thus chose 10 h^{-1} kpc to minimize any seeing-dependent effects and at the same time maximize distance accuracy. For comparison, Hoessel (1980) used a 9.6 h^{-1} kpc aperture. The metric magnitudes at the survey redshift limit change by only ~ 0.002 mag, independent of α, when the images are convolved with a typical stellar point-spread function. The effects of seeing on the measured photometry at $r_m = 10\ h^{-1}$ kpc are, thus, negligible, which is not surprising, since the metric aperture radius is 14".99 at the survey limit of $z = 0.05$.

4.2. *BCG Properties and Parameter Correlations*

The central regions of BCGs interior to the metric aperture appear to contain similar stellar populations. Not only are the absolute metric magnitudes constant to within $\sim 24\%$ (after correcting for the L_m-α relationship), but the $B-R_c$ colors are impressively constant—the average $B-R_c$ color corrected for extinction and K-dimming is 1.507 ± 0.006 mag, with a dispersion of only 0.055 mag, after the random errors in the photometry are accounted for. This is in excellent agreement with Schneider et al. (1983a), who found BCGs to have a dispersion of only 0.055 mag in $g-r$. The K-dimming and extinction corrections are indeed important, however; trend lines in the Figures 5*a* and 5*b* show how the color would redden if extinction and K-dimming corrections had not been made. Figures 5*a*–5*d* show the $B-R_c$ color as functions of $E(B-V)$, redshift, L_m, and the residual from the quadratic L_m-α relation, respectively. Once corrected, the colors show no dependence on extinction or redshift, nor on BCG metric luminosity.

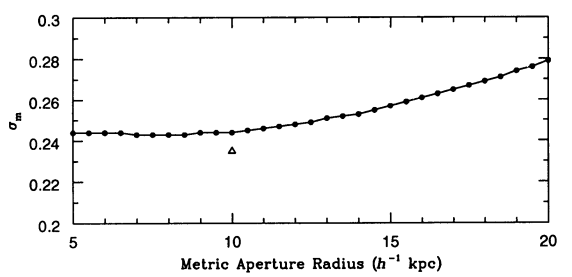

FIG. 4.—Scatter about the quadratic L_m-α relationship as a function of metric aperture radius.

The median color gradient, $d(B-R_c)/d \log r$, over the range 8–50 h^{-1} kpc is -0.031 with a scatter of 0.192. There is no systematic trend for the BCGs to become bluer or redder with radius. The most extreme BCG color gradient seen in our sample is for A3554, which has $\Delta(B-R_c) = 0.36$ between radii of 40 h^{-1} kpc and 10 h^{-1} kpc.

BCG metric luminosities and residuals from the best-fit quadratic L_m-α relationship are also independent of the BCG location within its host cluster. Figures 6*a* and 6*b* show, respectively, the residuals as functions of BCG radial velocity offset and projected separation from the cluster center.

If BCGs just represent the brightest members drawn from a normal cluster luminosity function, then one might expect the BCG luminosity to depend on cluster richness (Scott 1957). However, the constancy of the BCG metric luminosity over an order of magnitude in cluster galaxy surface density argues against this hypothesis, as does the analysis of Tremaine & Richstone (1977). Figures 7*a*–7*d* show cluster richness (as represented by the Abell/ACO galaxy count) as functions of the BCG $B-R_c$ color, α-parameter, absolute R_m magnitude, and the residual from the quadratic L_m-α relation, respectively. Again, there are no significant trends between richness and any of these parameters. Note that the metric magnitudes in Figure 7*c* are *not* corrected for the L_m-α relationship, demonstrating that BCG metric luminosity is simply not dependent on cluster richness (alternatively, the Abell galaxy count may not be a good indicator of richness, but for $z \leq 0.05$ this is not likely). Of course, our sample contains only 12 clusters with Abell richness class greater than 1, and, hence, our constraints on the dependence of BCG parameters on richness are really limited to clusters with $R \leq 1$.

Finally, we look for correlations with BCG ellipticity, which is measured from the luminosity-weighted average of isophotes falling within the 10 h^{-1} kpc metric radius (cf. Ryden, Lauer, & Postman 1992). Figures 8*a*–8*d* show BCG ellipticity as functions of BCG $B-R_c$ color, α, L_m, and the residual from the quadratic L_m-α relation, respectively. The ellipticity is weakly correlated with both the metric luminosity and α (but since there exists an L_m-α relationship, this dual correlation is expected). The linear correlation coefficients are 0.306 and -0.241, respectively, for the e-α relation and the e-L_m relation. The probabilities that a random sample of 119 points would produce correlation coefficients as large as this are 7.2×10^{-4} and 8.4×10^{-3}, respectively. Adding ellipticity as an independent variable does not significantly improve the dispersion in metric luminosity, however (with ellipticity, $\sigma_m = 0.242$ mag). Consequently, we expect and find that the residuals from the quadratic L_m-α relation are not significantly correlated with ellipticity.

In summary, residuals from the quadratic L_m-α relationship are independent of BCG color, BCG location, BCG ellipticity,

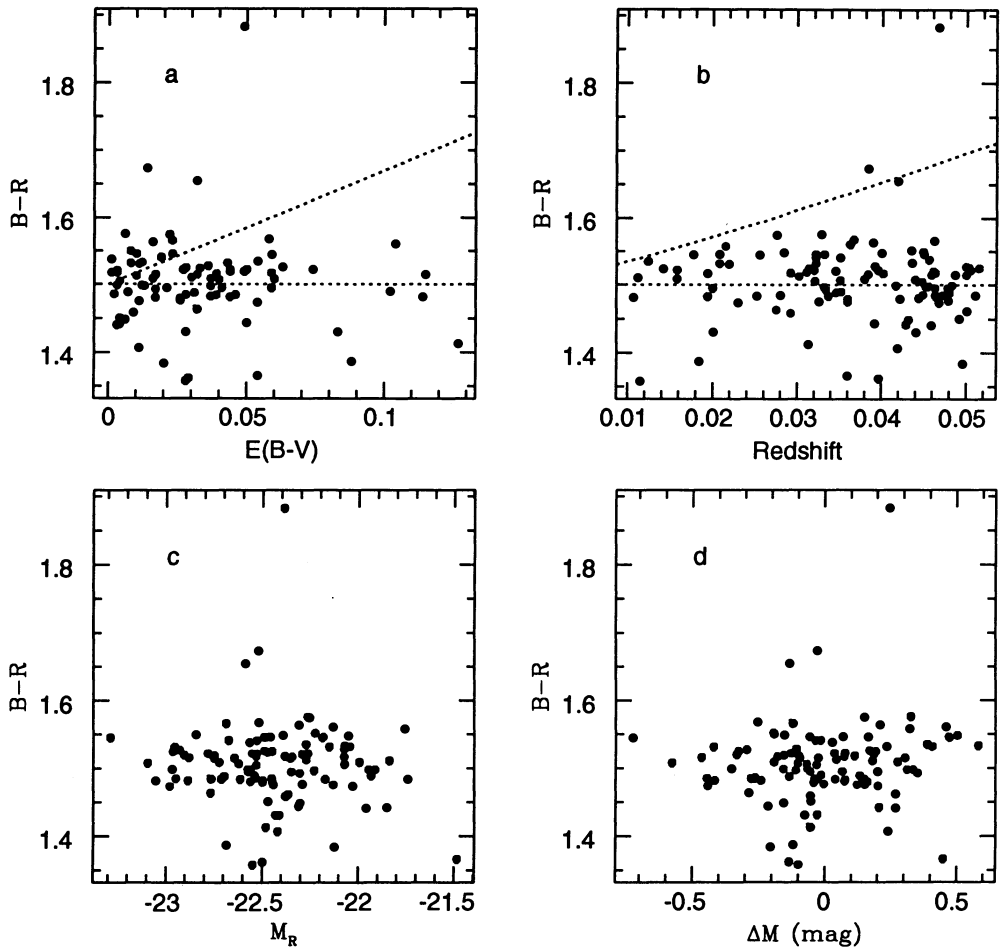

FIG. 5.—(*a*) BCG $B-R_c$ color as a function of $E(B-V)$. The rising dashed line shows the expected reddening when no extinction correction is applied. (*b*) BCG $B-R_c$ color as a function of redshift. The rising dashed line shows the expected reddening when no K-dimming correction is applied. (*c*) BCG $B-R_c$ color as a function of absolute R_m magnitude. (*d*) BCG $B-R_c$ color as a function of the residual from the quadratic L_m-α relationship.

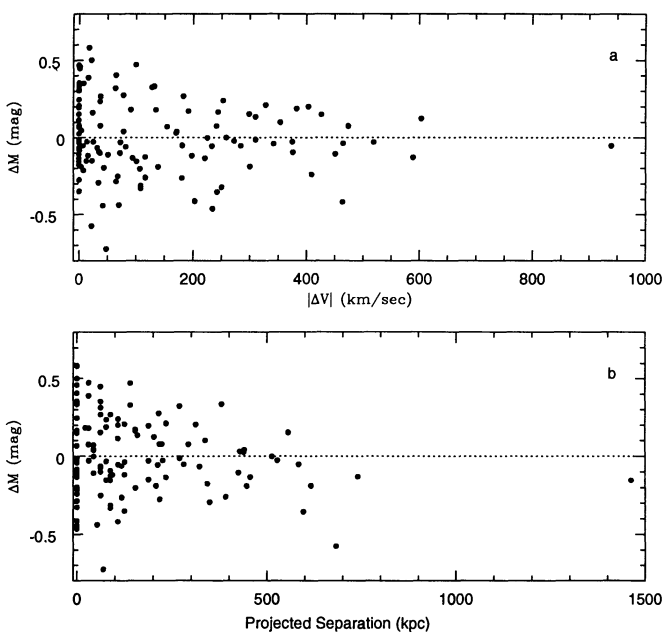

FIG. 6.—(*a*) Residual from the quadratic L_m-α relationship as a function of the BCG radial velocity offset from the mean cluster redshift. (*b*) Residual from the quadratic L_m-α relationship as a function of the BCG projected separation from the published Abell/ACO cluster center.

and cluster richness. We note in passing, however, that there is evidence to suggest that the internal BCG stellar velocity dispersion is correlated with the residuals. A full investigation of this correlation and its effect on distance determination will be presented in a subsequent paper.

4.3. *Computing Estimated Redshifts for BCGs*

For all of our discussion here, and in Paper I, we have assumed that the cluster redshifts give the best initial distance estimate to the BCGs with the L_m-α relationship providing independent information on BCG distances that we use to statistically correct for departures of the clusters from a perfect Hubble flow. One can use the L_m-α relationship directly as well, however, to estimate the redshift of any elliptical BCG. As we discuss below, this technique may provide the best distances to clusters lacking proper redshifts.

We estimate redshifts by measuring the brightness of the BCG through a set of apertures, finding the best aperture to place the BCG on the nominal L_m-α relationship. We begin by selecting one of the apertures (the initial choice is not important), assuming that it corresponds to the 10 h^{-1} kpc metric radius. The aperture choice thus implies the redshift (by eq. [1] in § 4.1), the corresponding K-correction, and hence the absolute metric magnitude; α is also measured at the aperture selected. We then compare the derived absolute metric magnitude with the expected absolute metric magnitude for the

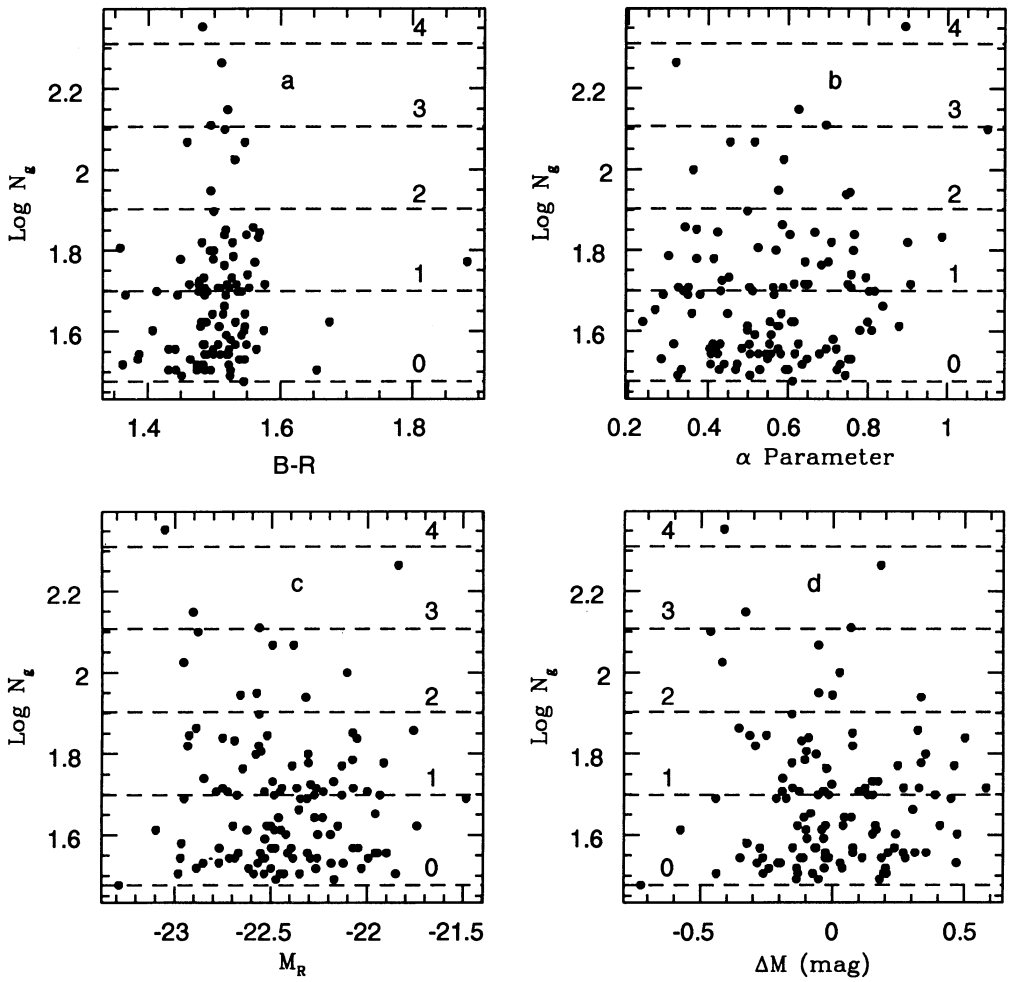

FIG. 7.—(*a*) Cluster richness as a function of BCG $B-R_c$ color. The horizontal dashed lines represent Abell richness class boundaries. (*b*) Cluster richness as a function of α. (*c*) Cluster richness as a function of L_m. (*d*) Cluster richness as a function of the residual from the quadratic L_m-α relationship.

observed α based on the L_m-α relationship (eq. [2] in § 4.1; valid for the Cousins R_c band, $H_0 = 80$, $q_0 = 0.5$). If the metric aperture is too small, then the BCG redshift will be initially overestimated, and the derived metric luminosity will be brighter than that expected for a BCG really at that redshift. Conversely, if the BCG redshift is underestimated (aperture too big), the derived metric luminosity will be fainter than expected. The size of the error leads to a revised aperture choice. In practice, the proper aperture, and thus redshift estimate, can be found precisely by performing an interpolation between a series of aperture radii (providing that the apertures selected bracket the true metric radius). The final aperture is the one that gives an absolute metric magnitude that exactly matches the prediction from the L_m-α relationship for the α measured. We note that the quadratic fit to the L_m-α relationship in the Johnson *B* band differs from eq. (2) (§ 4.1) only in the zero point—the first- and second-order coefficients are the same to within the errors. Consequently, this redshift estimation technique is applicable over the full optical bandpass.

The errors in the estimated redshifts depend on α, as has already been discussed by Gunn & Oke (1975). This can be seen as follows. Near the metric radius, the estimated metric luminosity, L_e, varies with estimated metric radius, r_e, away from the nominal values as

$$L_e = L_m\left(\frac{r_e}{r_m}\right)^{\alpha} .$$

At any α, this can be cast in terms of surface brightness as

$$\mu_e = \mu_m\left(\frac{r_e}{r_m}\right)^{\alpha-2} ,$$

where μ_m is the average metric surface brightness for the given α. Now the dispersion in L_m, σ_m, implies an identical dispersion in μ_m. From the equation above, we can see that as μ_e varies from the nominal μ_m the ratio of the estimated distance, D_e to the nominal value will be

$$\frac{D_e}{D_m} = \left(\frac{\mu_e}{\mu_m}\right)^{1/(\alpha-2)} .$$

For small σ_m, this implies that the relative redshift error is

$$\Delta z/z \approx \sigma_m/(2-\alpha) .$$

The limits of this expression are simple to understand. For $\alpha = 0$ (a point source) the flux is simply proportional to D^{-2} as

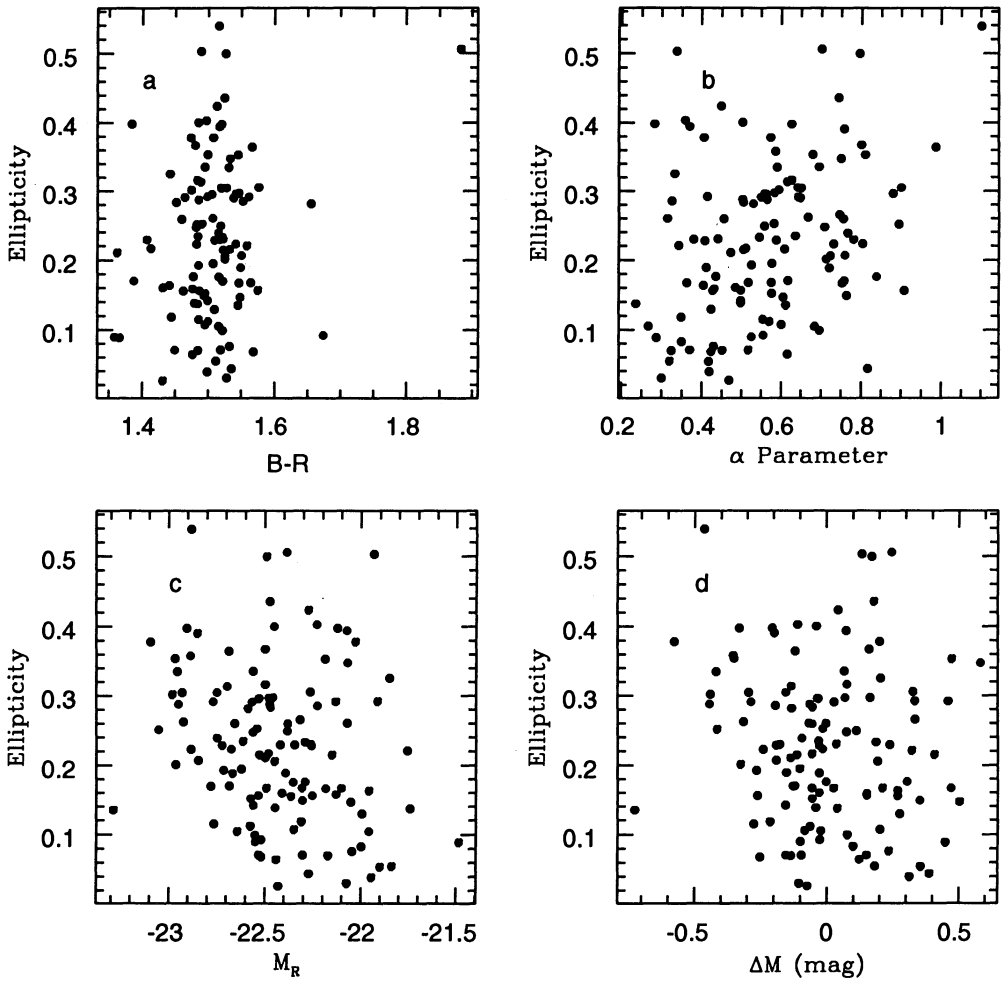

FIG. 8.—(*a*) BCG ellipticity as a function of BCG $B-R_c$ color. (*b*) BCG ellipticity as a function of α. (*c*) BCG ellipticity as a function of L_m. (*d*) BCG ellipticity as a function of the residual from the quadratic L_m-α relationship.

expected. For $\alpha = 2$ (a constant surface brightness sheet), the flux is simply proportional to the area of the aperture and is insensitive to distance. For the current sample, $\bar{\alpha} = 0.57$ and $\sigma_m = 0.244$ mag, implying a mean distance uncertainty of $\pm 17\%$ per BCG.

Figure 9 shows the estimated redshift (as derived above) as a function of the observed redshift for the 119 BCG in our sample. The solid line is $z_{est} = z_{obs}$; the dashed lines denote the $\pm 17\%$ limits. The data are plotted in log-log coordinates to demonstrate that the fractional distance error is independent of redshift. The mean and standard deviations for $(z_{obs} - z_{est})/z_{obs}$ are -0.012 and 0.173, respectively. Note the excellent agreement between the predicted distance uncertainty and the observed dispersion in $(z_{obs} - z_{est})/z_{obs}$. The scatter about the line $z_{est} = z_{obs}$ is relatively insensitive to α, although the error in any given BCG redshift estimate is, of course, dependent on its α-value. The best-fit line is

$$z_{est} = (0.965 \pm 0.055) z_{obs} + (0.002 \pm 0.002) ,$$

with a linear correlation coefficient of 0.849.

The L_m-α redshift estimation scheme is superior to other photometrically based redshift estimators for clusters (at least

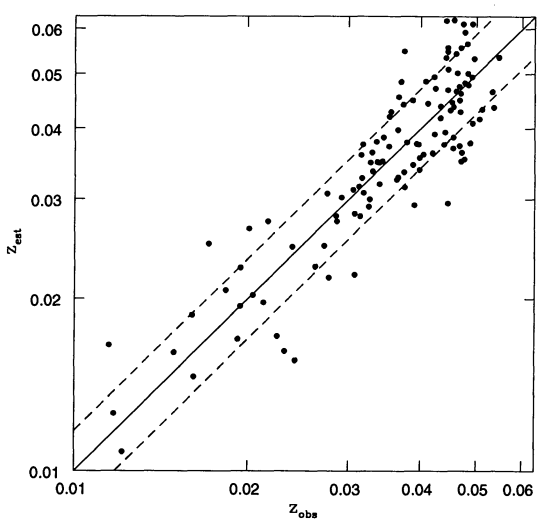

FIG. 9.—Estimated cluster redshift as a function of the observed cluster redshift. The redshift estimates are derived solely from the BCG photometry. The dashed lines show the $\pm 17\%$ limits corresponding to the average expected BCG distance error.

to $z = 0.05$ and most likely to much higher redshifts as long as evolution effects within the central 10 h^{-1} kpc remain small compared to the 0.244 mag cosmic scatter). For comparison, the mean and standard deviation for $(z_{obs} - z_{est})/z_{obs}$ using Leir & van den Bergh (1977) redshift estimates for Abell clusters with $z_{obs} < 0.055$ are -0.125 and 0.299, respectively. The larger mean indicates a significant bias in the redshift estimate (the error in the mean is ± 0.038), and the scatter is about twice as big as that for the BCG method. For $z > 0.1$, photometrically derived redshift estimates from the tenth-ranked cluster galaxy become seriously biased due to interloper contamination (Postman et al. 1985). While BCG selection can also be problematic when redshift data are not available, the narrow color range and elliptical morphology can make their selection much more robust against foreground and background confusion.

4.4. *The Second-ranked Galaxy*

As part of our program, we considered the question of whether the *second*-ranked galaxy (SRG) in a cluster might also be a good standard candle. For example, in A1656 (Coma) the R_c-band metric magnitude of the BCG (NGC 4889) is 0.41 mag brighter than the SRG (NGC 4874), but NGC 4874 is itself brighter than many of the BCGs from other clusters. If the L_m-α relationship were just a property of the most luminous elliptical galaxies, then perhaps it might also be valid for the brighter SRGs. This possibility is especially intriguing as one might expect that many of the present SRGs were once BCGs in their own right prior to their original clusters merging with their neighbors.

During the course of our survey, we obtained CCD data for 30 SRGs (see Table 7) as part of the BCG selection process, but also with the above issues in mind. Figure 10 shows where these SRGs lie in the L_m-α plane. Each SRG (*solid square*) is linked by a line to its corresponding BCG (*open square*). The BCG L_m-α relationship from Figure 1 is also plotted for comparison. Unfortunately, it appears that SRGs are distinct from BCGs in their structural properties. If SRGs were simply fainter versions of BCGs, then one might expect that the SRGs would be displaced along the mean L_m-α relation toward lower α-values (fainter absolute magnitudes). While this is true for a few SRGs, in most cases exactly the opposite shift is seen—the SRGs typically have *larger* α-values than the BCGs, despite their lower metric luminosities.

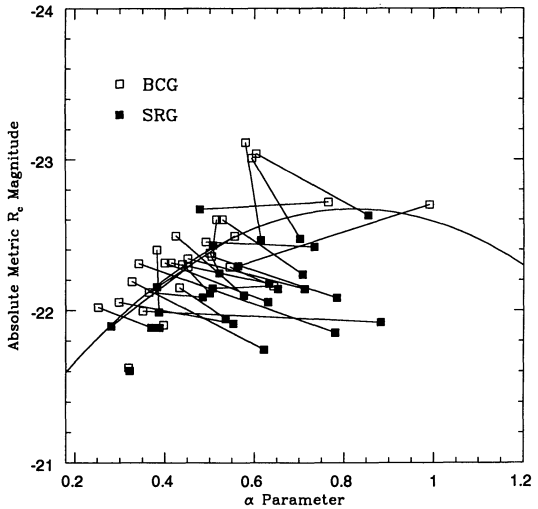

FIG. 10.—Luminosity of SRGs as a function of α. Each SRG (*solid square*) is linked by a line to its corresponding BCG (*open square*). The BCG L_m-α relationship from Fig. 1 is also plotted.

TABLE 7

SECOND-RANKED GALAXY OBSERVATIONS

Abell	R.A. (J2000)	Decl.	$M_2 - M_1$	α	cz	σ	Notes
076-2	$00^h39^m33^s.51$	+06°48′52″.5	0.334	0.383	11916	31	I1566
119-2	00 56 25.53	−01 15 44.9	0.046	0.478	11575	250	
147-2	01 08 11.85	+02 11 35.6	0.393	0.577	12587	75	
533-2	05 01 35.99	−22 36 03.1	0.132	0.522	14642	34	
539-2	05 16 37.34	+06 26 28.0	0.274	0.785	8318	47	
548-A.....	05 48 38.48	−25 28 38.4	0.033	0.734	11942	57	
576-1	07 21 32.51	+55 45 25.9	0.141	0.553	12177	100	
1142-1	11 00 57.45	+10 30 20.9	0.144	0.653	11150	43	NGC 3492A
1228-2	11 21 42.70	+34 21 47.2	0.207	0.536	10578	39	I2744
1644-2	12 57 49.30	−17 32 44.5	0.405	0.564	14013	50	
1656-2	12 59 35.65	+27 57 33.0	0.412	0.855	7176	15	NGC 4874
1736-2	13 26 48.69	−27 08 36.9	0.650	0.614	13719	49	
1983-2	14 52 55.24	+16 42 09.1	0.457	0.781	13581	52	
2152-2	16 05 26.57	+16 26 32.8	0.411	0.387	...	...	
2197-2	16 27 41.19	+40 55 36.8	0.537	0.702	9408	77	NGC 6160
2247-2	16 50 59.06	+81 34 28.5	0.139	0.633	11409	98	
2572-1	23 18 30.39	+18 41 21.1	0.363	0.708	11610	150	NGC 7597
2657-1	23 44 57.44	+09 11 30.7	0.074	0.883	12361	46	
2806-1	00 40 12.92	−56 09 15.0	0.260	0.631	8244	49	
2881-2	01 10 54.46	−17 11 51.6	0.017	0.388	12665	38	
2911-A.....	01 24 44.69	−38 07 42.3	0.017	0.322	5826	23	NGC 534
3374-2	05 56 54.98	−21 15 06.0	0.133	0.370	14502	36	
3389-2	06 21 26.41	−64 59 37.1	0.170	0.507	8027	44	
3564-2	13 34 11.98	−35 20 14.9	0.193	0.501	...	...	
3566-1	13 40 13.34	−35 40 30.2	0.033	0.485	...	...	
3570-1	13 46 47.33	−37 54 28.4	0.448	0.622	11237	74	
3733-2	21 01 37.58	−28 01 56.2	0.013	0.507	11505	107	NGC 6998
3747-2	21 08 28.99	−43 29 24.5	0.390	0.281	5086	30	
4038-1	23 47 44.96	−28 08 31.4	0.200	0.713	7940	150	

We emphasize that selection of our SRG sample was highly biased, but in a way that we had presumed would strongly favor SRGs that resembled BCGs; SRGs that were dramatically fainter than the BCGs were systematically excluded. The average $M_1 - M_2$ for these 30 clusters is -0.242 mag, and the scatter about the mean absolute SRG metric magnitude is 0.255 mag. The small offset and artificially small dispersion (Schneider, Gunn, & Hoessel 1983b get a dispersion of 0.55 mag for a complete SRG sample) show that many of the SRGs selected will be brighter than the fainter BCGs. While a complete sample might show the faintest SRGs to fall on the low end of the L_m-α relationship, clearly the brightest SRGs do not fit it at all. The possibility that bright SRGs are fundamentally different from BCGs was also raised by Ryden et al. (1993), who find that these same SRGs are both rounder and have a narrower axis-ratio dispersion than BCGs and ordinary elliptical galaxies. These observations suggest different formation scenarios and/or merging histories for BCGs and these SRGs. In this context, it is interesting to note that Hoessel (1980) argued that the L_m-α relationship was just the track followed by bright ellipticals as they grew by cannibalism (Hausman & Ostriker 1978). This scenario, however, will not work for SRGs, since α is expected to increase rather than decrease as the galaxies accrete their fellow cluster members. The results are intriguing enough to make acquisition of photometric data for a complete SRG sample worthwhile and, indeed, a necessity to fully determine the status of SRGs as standard candles.

5. SUMMARY

We have completed a reinvestigation of BCGs as distance indicators with the specific goal of establishing a frame suitable for measuring galaxy bulk flows at large distances. We emphasize the following aspects of our sample selection and observations:

1. Our sample covers the full sky, except for regions with $|b| < 15°$. Further, the sample is volume limited and as such includes all Abell clusters known with $z \leq 0.05$. In contrast, previous BCG samples have been limited to clusters observable from the north and were not complete or volume limited.
2. We have performed our own BCG selection. The final BCG selected for a given cluster is the galaxy that has the greatest flux within the metric aperture, regardless of position within the cluster. We have also recalculated the redshifts of all clusters, giving the BCGs high weight due to their preferential location at the kinematic centers of the clusters.
3. Large-format CCD cameras were used to ensure the best sky subtraction. Multi-isophote fitting software was used to remove other cluster galaxies and stars seen in projection against the BCGs.
4. A network of overlap galaxy observations ensures that the photometric observations are homogeneous over the sample. We find that all runs have zero points consistent to 0.01 mag and that the random photometric error in the R_c-band metric luminosities is 0.014 mag. We thus expect that any systematic errors in the velocity solutions presented in Paper I, due to photometric calibration errors, will be limited to 75 km s^{-1}.

We have confirmed the existence of the Hoessel (1980) L_m-α relationship for BCGs. The L_m-α relationship appears to be linear for small α, flattening off, however, as α increases. The L_m-α relationship is described by a second-order curve. We have adopted $r_m = 10\ h^{-1}$ kpc, after exploring the dependence of the BCG cosmic luminosity scatter, σ_m as a function of r_m. The basic scatter in L_m is 0.327 mag, which decreases to 0.244 mag, once the relationship between L_m and α is accounted for. The scatter about the L_m-α relationship for $\alpha < 0.6$ decreases to 0.181 mag. The distributions of L_m and L_m-α residuals are both consistent with single Gaussian distributions. The L_m-α relationship can be used to estimate BCG redshifts with 17% mean accuracy. This is as expected, given $\sigma_m = 0.244$ and the mean BCG $\bar{\alpha} = 0.57$. We have conducted an extensive search for additional "second parameters" that might be used to minimize σ_m further as follows:

1. There are no correlations between BCG $B-R_c$ color and L_m, L_m-α residuals, redshift, extinction, BCG ellipticity, or cluster richness, after extinction and K-corrections have been applied.
2. There are no correlations between L_m-α residuals and BCG offsets from the mean cluster velocity or projected cluster center. Both L_m and L_m-α residuals are uncorrelated with cluster richness.
3. BCG ellipticity may weakly correlate with L_m and L_m-α residuals, but is not correlated with α.
4. We have obtained central stellar velocity dispersion measurements for all 119 BCGs. The BCG internal velocity dispersions may correlate with L_m-α residuals. We are currently investigating this and will report our results in a subsequent paper.

We conclude that BCGs are a highly homogeneous population, making them suitable for statistical studies of galaxy peculiar velocities on large scales. We are currently extending the cluster frame defined in Paper I to $z = 0.08$. This program includes the observation of approximately 500 additional BCGs. The deeper sample is well suited to further investigation of the BCG properties considered in this paper.

We are greatly indebted to several of our colleagues who made key contributions to this project. We thank Ofer Lahav and Jim Gunn for useful conversations that helped define the observational program. John Huchra provided invaluable support by supplying essential galaxy redshift data from the CfA Redshift Catalog and, along with Ann Zabludoff, obtained several new galaxy redshifts at our request. Andy Fruchter provided photometric calibrations for a few of the images, and John Tonry obtained images of a few galaxies missed during our own runs. Dave Burstein, Tina Bird, Sandy Faber, Jim Gunn, Bohdan Paczyński, and Michael Strauss provided many critical and constructive discussions for which we are most grateful. This program was based on imaging observations obtained exclusively at the facilities of the National Optical Astronomy Observatories—we thank the Kitt Peak National Observatory and Cerro Tololo Inter-American Observatory TACs for their generous grants of observing time. We also thank the KPNO and CTIO staff for the tremendous support we received throughout this program. M. P. was supported by NASA grant NAGW-2166 and by the STScI Director's Discretionary Research Fund. BCG identifications and astrometry were obtained using the Guide Stars Selection System Astrometric Support Program developed at the STScI.

REFERENCES

Abell, G. O. 1958, ApJS, 3, 211
Abell, G. O., Corwin, H. G., & Olowin, R. P. 1989, ApJS, 70, 1 (ACO)
Bhavsar, S. P. 1989, ApJ, 338, 718
Burstein, D., & Heiles, C. 1984, ApJS, 54, 33
Colless, M., Burstein, D., Wegner, G., Saglia, R. P., McMahon, R., Davies, R. L., Bertschinger, E., & Baggley, G. 1993, MNRAS, 262, 475
Gunn, J. E., & Oke, J. B. 1975, ApJ, 195, 255
Hausman, M. A., & Ostriker, J. P. 1978, ApJ, 224, 320
Hoessel, J. G. 1980, ApJ, 241, 493
Hoessel, J. G., Gunn, J. E., & Thuan, T. X. 1980, ApJ, 241, 486
Hoessel, J. G., & Schneider, D. P. 1985, AJ, 90, 1648
Huchra, J. P. 1991, private communication
———. 1992, private communication
Huchra, J. P., Geller, M. J., Clemens, C., Tokarz, S., & Michel, A. 1992, Bull. d'Information du Centre des Données Astron. Strasbourg, 41, 31
Humason, M. L., Mayall, N. U., & Sandage, A. R. 1956, AJ, 61, 97
James, P. A., Joseph, R. D., & Collins, C. A. 1987, MNRAS, 229, 53
Landolt, A. U. 1983, AJ, 88, 439
Lasker, B. M., Sturch, C. R., McLean, B. J., Russell, J. C., Jenkner, H., & Shara, M. M. 1990, AJ, 99, 2019
Lauer, T. R. 1986, ApJ, 311, 34
———. 1988, ApJ, 325, 49
Lauer, T. R., & Postman, M. 1992, ApJ, 400, L47
Lauer, T. R., & Postman, M. 1994, ApJ, 425, 418 (Paper I)
Leir, A. A., & van den Bergh, S. 1977, ApJ, 221, 383
Lucey, J. R., & Carter, D. 1988, MNRAS, 231, 15P
Postman, M., Huchra, J. P., & Geller, M. J. 1992, ApJ, 384, 404
Postman, M., Huchra, J. P., Geller, M. J., & Henry, P. J. 1985, AJ, 90, 1400
Press, W. H., Flannery, B. P., Teukolsky, S. A., & Vetterling, W. T. 1986, Numerical Recipes (Cambridge: Cambridge Univ. Press)
Quintana, H., & Lawrie, D. G. 1982, AJ, 87, 1
Ryden, B. S., Lauer, T. R., & Postman, M. 1993, ApJ, 410, 515
Sandage, A. 1972a, ApJ, 173, 485
———. 1972b, ApJ, 178, 1
———. 1975, ApJ, 202, 563
Schneider, D. P., Gunn, J. E., & Hoessel, J. G. 1983a, ApJ, 264, 337
———. 1983b, ApJ, 268, 476
Scott, E. L. 1957, AJ, 62, 248
Tonry, J., & Davis, M. 1979, AJ, 84, 1511
Tremaine, S. D., & Richstone, D. O. 1977, ApJ, 212, 311
Tully, R. B. 1987, ApJ, 323, 1
Whitford, A. E. 1971, ApJ, 169, 215
Zabludoff, A. I. 1992, private communication
Zabludoff, A. I., Geller, M. J., Huchra, J. P., & Vogely, M. S. 1993, AJ, 106, 1273
Zabludoff, A. I., Huchra, J. P., & Geller, M. J. 1990, ApJS, 74, 1